

## **Historic, Archive Document**

Do not assume content reflects current scientific knowledge, policies, or practices.





United States  
Department of  
Agriculture

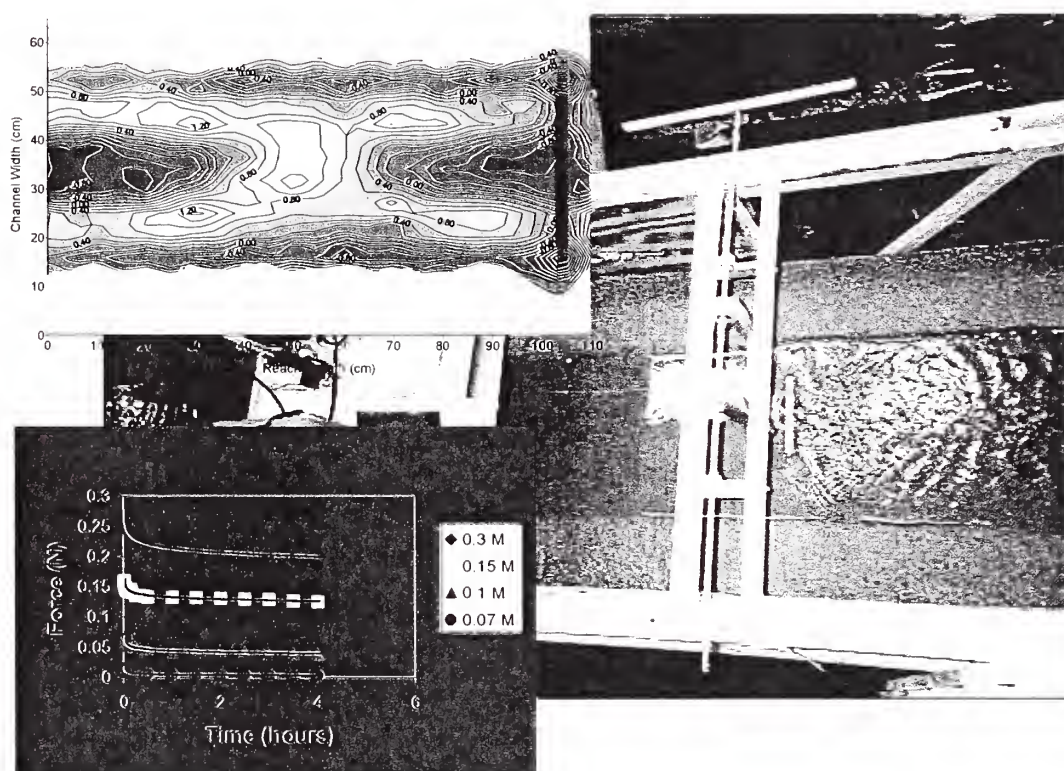


Agricultural  
Research  
Service

Department of  
Geography  
Nottingham University  
United Kingdom

Channel & Watershed Processes Research Unit  
National Sedimentation Laboratory  
Oxford, Mississippi 38655

## An Experimental Study of Alluvial Channel Response to Large Woody Debris



By N.P. Wallerstein, C.V. Alonso, S.J. Bennett & C.R. Thorne

Research Report No. 10

January 1999





United States  
Department of  
Agriculture

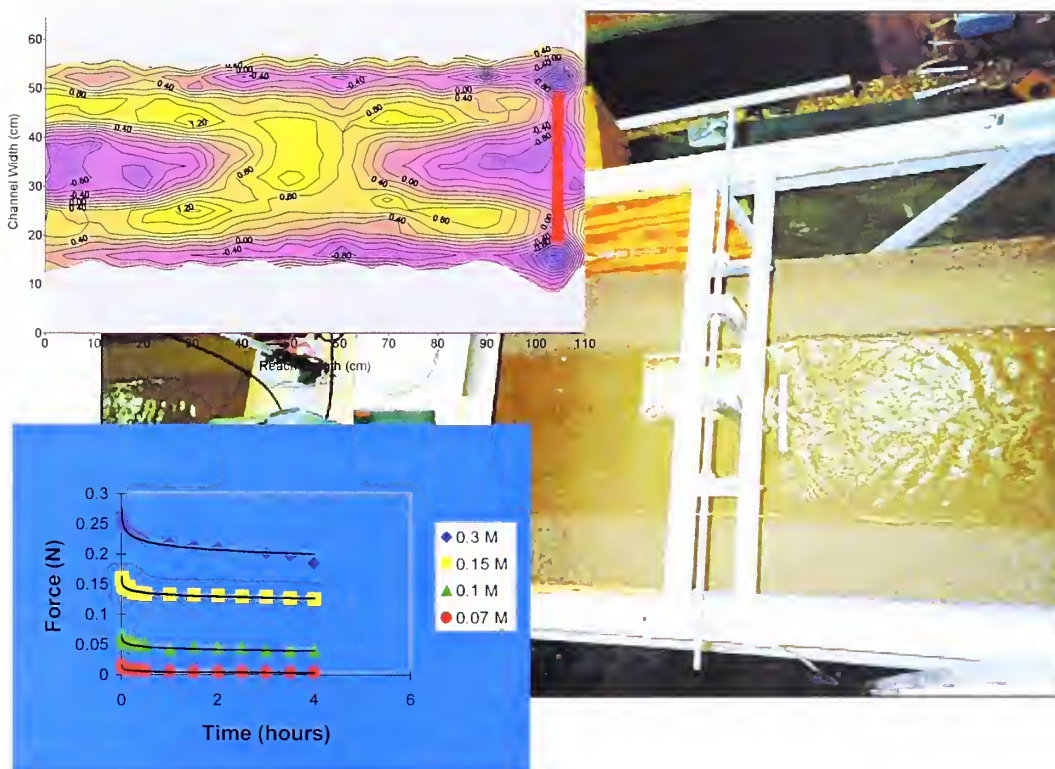


Agricultural  
Research  
Service

Department of  
Geography  
Nottingham University  
United Kingdom

Channel & Watershed Processes Research Unit  
National Sedimentation Laboratory  
Oxford, Mississippi 38655

## An Experimental Study of Alluvial Channel Response to Large Woody Debris



By N.P. Wallerstein, C.V. Alonso, S.J. Bennett & C.R. Thorne

Research Report No. 10

January 1999



## Table of Contents

Acknowledgements	iv
List of Figures	v
List of Tables	vii
List of Plates	viii
Chapter 1: Introduction	1
Chapter 2: Literature concerning the hydraulic impact of LWD	2
2.1 Effect of LWD on stage/discharge relationships, the hydrograph and flood frequency	2
2.2 Modeling the impact of LWD on flow afflux	3
2.3 Effect of LWD on channel roughness	6
2.4 Flume techniques	9
Chapter 3: Similarity in model scaling	10
3.1 Basic principles	10
3.2 Secondary scale ratios	12
3.3 Influence of viscous forces	13
3.4 Scaling channel boundary resistance in fixed bed models	15
3.5 Scale distortion	17
3.6 Moveable bed models	18
Chapter 4: Abiaca Creek scaling method	21
Chapter 5: Flume design and construction	33
Chapter 6: Description of flume results	40
6.1 Introduction	40
6.2 Expansion of flume results to prototype dimensions	40
6.3 Limitations of the flume model	41
Chapter 7: Discussion of Results	44
7.1 Drag coefficient calculations for simulated debris elements	44
7.2 Selection of drag coefficient values	48
7.3 Estimation of friction factor due to LWD	49
7.4 Drag force on LWD elements in the model	51





7.5 Drag force on LWD elements in the prototype	52
7.6 Incident flow velocity on LWD elements in the model	55
7.7 Incident flow velocity on LWD elements in the prototype	56
7.8 Conclusions from the hydraulic data	57
7.9 Geomorphic results: Flume	58
7.10 Geomorphic Results: Prototype	66
Chapter 8: Conclusions	72
Appendix	74
References	75



## **Acknowledgements**

The authors wish to thank the USDA Agricultural Research Service, National Sedimentation Laboratory, Oxford, Mississippi and the Department of Geography, Nottingham University, England for funding this research.



## List of Figures

1: Definition sketch of LWD model by Gippel et al. (1992)	4
2: The relationship between $C_D$ and $Re$ for various objects (after White, 1994)	14
3: The Shields entrainment function (modified from Vanoni, 1966)	19
4: Cross section of flume channel (dimensions in meters)	24
5: Flow diagram of procedure for creating a Froude scaled mobile boundary flume model from a prototype river	31
6: Schematic diagram of LWD positions in the flume	35
7: Flume set-up	36
8: Strain gauge set-up	36
9: Element drag coefficient as a function of Reynolds number	47
10: Drag coefficient as a function of relative flow depth	48
11: Measured change in drag force over time on each LWD element in the flume model	52
12: Change in drag force over time on LWD elements in the prototype reach computed from the model data	53
13: Calculated change in velocity over time approaching LWD elements in the model flume	55
14: Change in LWD element approach flow velocity over time in the prototype reach computed from model data	56
15: Contour plots of relative depth change for the flume model: 0.07 m and 0.1 m debris elements	60
16: Contour plots of relative depth change for the flume model: 0.15 m and 0.3 m debris elements	61
17: Geomorphic impact of surface waves generated by LWD elements	62
18: Contour plots of relative depth change calculated for the prototype reach: Flow parallel and deflector debris elements	68
19: Contour plots of relative depth change calculated for the prototype reach: Dam and Underflow debris elements	69
20: Geomorphic adjustments to a simple trapezoidal channel caused by 4.2 and	



6 meter long LWD elements	70
21: Geomorphic adjustments to a simple trapezoidal channel caused by 9 and 18 meter long LWD elements	71





## List of Tables

1: Dimensions for important fluid mechanics variables	11
2: Important scale ratios	13
3: Hydraulic variables for prototype reach in Abiaca Creek at $Q_2$ discharge	21
4: Scaling factor values and main flume dimensions determined by Froude-Manning scaling	25
5: Comparison of model and prototype channel variables	30
6: LWD proportions	33
7: Prototype debris element dimensions	42
8: Drag coefficient on elements at a range of depths in infinite flow	46
9: Drag coefficient values used to solve equation 47	48
10: Calculation of Darcy-Weisbach friction factor due to LWD	50
11: Computation of Darcy-Weisbach friction factor in the Obion River and Tumut River (after Shields and Gippel, 1995)	50
12: Equations describing drag force decay on LWD elements	52
13: Equations describing drag force decay on LWD elements in the prototype	53
14: Equations describing incident velocity decay at each LWD element in the model	55
15: Equations describing incident velocity decay on LWD elements in the prototype	57



## **List of Plates**

1: Model channel, showing scraper plate and pre-run channel geometry	37
2: Looking downstream along surface of channel, testing 0.1 m element	37
3: Experimental set-up, showing pivot arm and balance. Run with 0.1 m element	39
4: Force gauge set-up in fixed boundary flume to calibrate drag coefficient values for each element	44
5: Flow disturbance created by the 0.15 m debris element	62
6: Channel adjustment caused by the 0.3 m debris element	65



## **1 Introduction**

Field investigation in Northern Mississippi has demonstrated that the impact of LWD jams changes downstream through the channel network. This downstream change is conceptualized in the Debris Jam Classification Model (see Wallerstein et al., 1997). It is very difficult, however, to precisely determine which components of channel geomorphology are attributable to LWD influences, and which are caused by other, more dominant influences such as channel incision processes. It is also difficult to determine cause and effect when assessing the true geomorphic impact of LWD in streams.

In order to overcome the problem of interpretation, a flume model offers an excellent tool for more accurately determining the hydraulic forces exerted upon LWD elements and the impact of energy dissipation around the elements upon the channel boundary. In order to obtain meaningful experimental results it was necessary to create a scale model of a field site where survey of LWD-induced channel change had been conducted, so that model results could be assessed against field data. This report presents an overview of research carried out by others on the hydraulic effects of LWD, the theory of scale physical modeling, the derivation of parameters for the model created, a discussion of the parameters measured and their relative importance, and the presentation and analysis of the results obtained.



## **2 Literature Review of Hydraulic Impacts of LWD**

Previous studies have investigated the effect of LWD on runoff hydrographs, velocity distributions, water surface profile, and channel roughness.

### **2.1 Effect of LWD on stage/discharge relationships, the hydrograph and flood frequency**

LWD clearly influences the direction and magnitude of flow currents within stream flow, but few data have been documented in the literature. Swanson and Leinkaemper (1978) produced detailed maps of debris jams indicating flow direction. Smith and Shields (1992) reported that the removal of LWD from a river 18 to 23 m wide and 3.5 to 4.5 m deep produced more uniform flow, with less of the channel occupied by eddies or regions of reduced velocity.

LWD is often removed from channels because it is believed this will significantly reduce channel roughness which will, in turn, produce a higher mean velocity and increase in-bank channel flow capacity. There is some evidence to support this assumption. For example, Smith and Shields (1992) measured the mean velocity in two cleared reaches of the Obion River, Tennessee to be 0.4 m/s and 0.34 m/s respectively, while in an uncleared reach of the same river the mean velocity was 0.27 m/s. MacDonald and Keller (1987) found that there was a local increase in velocity by up to 250% as a result of LWD removal and decrease in sinuosity of the low-flow thalweg. According to Gippel et al. (1992), the Murray-Darling Basin Commission calculated a theoretical reduction in water level of 0.3 to 0.4 m after the removal of approximately 200 debris jams per kilometer. However, later analysis of flow records indicated a reduction of only 0.2 m. There should be a statistical reduction in the magnitude and frequency of overbank flooding where debris is removed from a channel because of the increased channel capacity. Bodron (1994) used a dynamic routing model to demonstrate changes in both stage and duration of flood events before and after LWD removal, using values of Manning's  $n$  calculated in the study by Smith and Shields (1992) at South Fork Obion River, West Tennessee. Despite the fact that the increase in channel cross-sectional area due to LWD removal was ignored, small reductions in flood height and duration were calculated based solely on the change in Manning's  $n$ . Bodron (1994) also





noted that flood stage would be reduced further if sediment accumulations at each jam site had been removed. However, according to Gippel et al. (1992), many claims regarding flood routing lack supporting data. It is even possible that LWD removal might increase downstream flood peaks because in the smoother channel the flood wave is less attenuated. Gregory et al. (1985) found that LWD ponds water which results in an increase in water depth and a decrease in velocity which, at low flows, influences travel time significantly. At high flows, however, the ponding effect of LWD is drowned out. Shields and Nunnally (1984) noted that because large accumulations of LWD have a damming effect on the flow which locally elevates the base level they can be treated as geometric elements within the channel, rather than simply as roughness elements, in backwater profile computations.

## **2.2 Modeling the impact of LWD on flow afflux**

Most studies of resistance to flow in rivers have concentrated on small-scale roughness, such as grain or bedform roughness where the size of the roughness element is small compared to the flow depth. LWD, on the other hand, represents a form of large-scale roughness (Petryk and Bosmajian, 1975). Flow conditions associated with the presence of LWD in streams varies from sub-critical to super-critical depending on the dimensions of the LWD and the depth of water.

Gippel et al. (1992) used the momentum equation to determine the hydraulic effect of LWD in terms of an afflux or backwater effect. If flow is subcritical (Froude number  $< 1$ ), then apart from local disturbance of the velocity profile, LWD only has an influence in the upstream direction. Quantifying the backwater effects is problematical because of the practical difficulties of directly measuring the afflux at debris jams. An alternative to direct measurement is prediction on the basis of a known relationship between afflux and more easily measured parameters. Gippel et al. (1992) used the results of a laboratory hydraulic study to develop a method of determining the afflux caused by LWD (see Figure 1).

Gippel et al. (1992) propose the use of the following equation to calculate afflux:



$$\Delta h = \frac{h_2 \left[ (F_r^2 - 1) + \sqrt{(F_r^2 - 1)^2 + 3C_D B F_r^2} \right]}{3} \quad (1)$$

where,  $\Delta h$  = afflux =  $h_1 - h_2$  (m), and the drag coefficient ( $C_D$ ) is given by

$$C_D = \frac{F_D}{\frac{1}{2} \rho v^2 A_D} \quad (2)$$

where,  $F_D$  = drag force (N),  $\rho$  = density of water (1000 kg/m<sup>3</sup>),  $v$  = mean approach velocity to object (m/s), and  $A_D$  = area of the LWD element projected in the flow direction (m<sup>2</sup>).

The Froude number ( $F_r$ ) is defined as:

$$F_r = \frac{v_2}{\sqrt{gh_2}} \quad (3)$$

where  $v_2$  = mean velocity at section downstream of the LWD (m/s), and  $h_2$  = water depth downstream of LWD (m)

The blockage ratio ( $B$ ) is defined as:

$$B = A_D / A \quad (4)$$

where  $A = w$  (channel width) x  $h_1$  = cross sectional area of flow (m<sup>2</sup>).

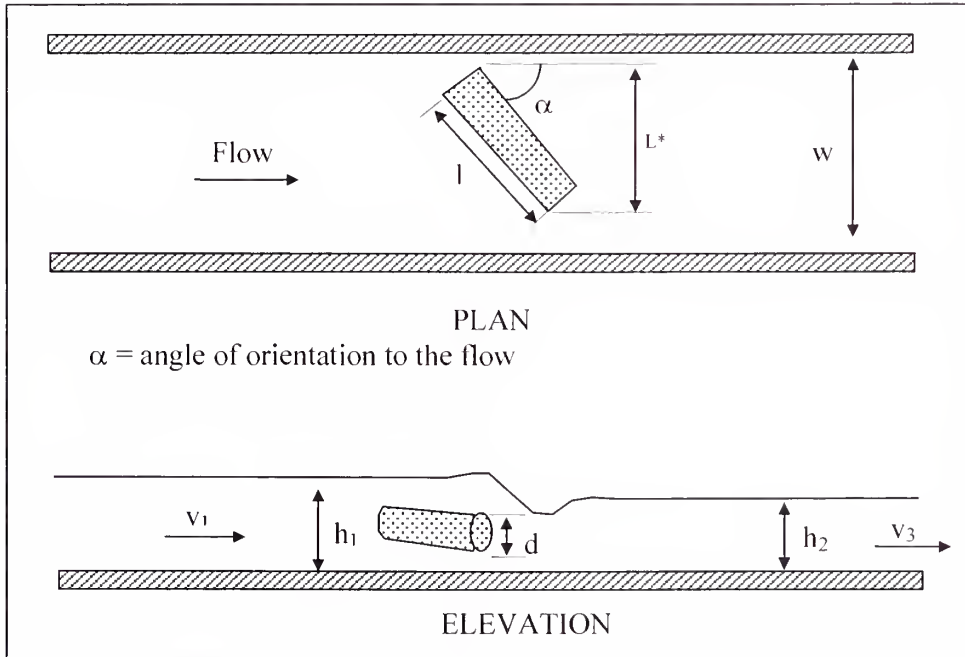


Figure 1: Definition sketch of LWD model by Gippel et al. (1992)



Thus, the afflux depends on  $F_r$ ,  $C_D$  and  $B$ . The Froude number can be calculated from direct measurement or from flow records.  $B$  can be found from a field survey.

The remaining problem centers on selecting an appropriate drag coefficient. The drag characteristics of a cylinder in infinite flow are well known (Petryk and Bosmajian, 1975). Less is known about drag on cylinders within boundaries where the “blockage effect” is significant and the drag coefficient is consequently increased. Gippel et al (1992) conducted experiments on LWD models to determine drag force, using a towing carriage and water tunnel. Froude number, LWD length to diameter ratio, and LWD distance from the bed all affected drag coefficient, but were much less important than the blockage effect, angle of orientation to the flow, and the shielding effect (i.e., one piece of LWD behind another). A suitable drag coefficient ( $C'_D$ ) for the LWD in question can be selected from their experimental results (Gippel et al. 1992, figures 3.8 or 3.12) on the basis of its overall shape and angle of orientation. The drag coefficient should then be adjusted for the blockage effect, which can be calculated using the following equation developed by Gippel et al. (1992) using their empirical data from flume studies:

$$C_D = C'_D (1-B)^{-3} \quad (5)$$

where  $C_D$  = adjusted drag coefficient, and  $C'_D$  = drag coefficient in infinite flow. These data are then substituted into equation 1 to calculate the afflux.

Predicted and measured afflux values resulting from the flume study were very closely correlated, and Gippel et al. (1992) concluded that the flume conditions did not seriously violate any of the assumptions in equation 1. The proposed method of afflux estimation was then applied to data collected from the Thomson River, Victoria and revealed that de-snagging would produce a reduction in stage of only 0.01 m at bankfull flow.

In conclusion the authors believe this method of backwater or afflux calculation due to individual LWD formations could be used as a tool to help determine whether the afflux reduction due to LWD removal would have a significant, positive impact. Conversely, this method could determine whether LWD could be left in place and perhaps, re-orientated,



lopped or even re-introduced where sympathetic rehabilitation management is desirable, without significant effect on high in-bank stages.

### 2.3 Effect of LWD on channel roughness

The Manning equation is based on a resistance coefficient that represents all sources of roughness in the channel and is defined as:

$$n = \frac{R^{2/3} S^{1/2}}{v} \quad (6)$$

where  $n$  = Manning's roughness coefficient,  $R$  = hydraulic radius (m), and  $S$  = energy slope. This equation is widely used by river engineers who select values of  $n$  from personal experience, tables in Chow (1959) or photographs in Barnes (1967). The range of  $n$  values in stream channels without LWD is between 0.025 and 0.15. For streams heavily congested with LWD, less than 30 m wide,  $n$  ranges from 0.075 to 0.15. Irregular and rough reaches of large streams have values of  $n$  from 0.035 to 0.10.

Manning's  $n$  has an empirical derivation, however, while the Darcy-Weisbach flow resistance equation has the advantage of being theoretically based (Richards, 1982). The Darcy-Weisbach  $f$  is defined as:

$$f = \frac{8gRS}{v^2} \quad (7)$$

where  $f$  = Darcy-Weisbach friction factor and  $g$  = acceleration due to gravity ( $9.81 \text{ m/s}^2$ ).

The effect of LWD on flow resistance varies as a function of relative flow depth. Bevan et al. (1979) found that when LWD is large in relation to flow depth the roughness coefficient is extremely high (Manning's  $n > 1$ ). As LWD is submerged it exerts less influence on flow resistance. Smith and Shields (1992) measured a large decrease in  $f$  as discharge increased. They also observed that friction factors for cleared and uncleared reaches converged at high in-bank flows. Indirect evidence to support these findings is provided by investigations of downstream hydraulic geometry which show that roughness generally decreases as channel size increases (Wolman, 1955). Petryk and Bosmajian (1975) derived the following equation





to predict  $n$  as a function of density of vegetation in the channel, hydraulic radius,  $n$  due to boundary roughness and a vegetation drag coefficient (in US units):

$$n = n_b \sqrt{1 + \frac{C_D \sum A_{Di}}{2gAL} \left( \frac{1.49}{n_b} \right)^2 \left( \frac{A}{P} \right)^{\frac{2}{3}}} \quad (8)$$

where  $n_b$  = Manning's boundary roughness coefficient excluding the effect of vegetation,  $C_D$  = drag coefficient for vegetation,  $A_{Di}$  = projected area of the  $i$ th plant in the streamwise direction ( $m^2$ ),  $L$  = length of the channel reach being considered (m), and  $P$  = channel wetted perimeter (m). In this formula the expression  $C_D \sum A_{Di} / AL$  represents the density of vegetation in the channel. A problem with this formula lies in selecting a value for the drag coefficient,  $C_D$ . Petryk and Bosmajian (1975) assumed a value of 1, but as mentioned previously this strictly only applies to cylinders in infinite flow. In streams, interference from nearby obstructions and the effect of blockage on the drag coefficient must also be considered. These effects are discussed further in section 6.3.

Manning's equation is also inapplicable in situations where there is a high degree of obstruction in the channel, particularly where  $n > 1$ . This is because  $n$  was empirically derived to describe open channel situations with fully turbulent flow where friction is controlled primarily by skin friction at the channel boundary. The equation attaches significance to the hydraulic radius which may be irrelevant if the channel is heavily choked with LWD. It was therefore considered inappropriate to use Petryk and Bosmajian's (1975) equation to determine average friction factor values for debris elements in the study reaches.

Smith and Shields (1992) studied the effects of varying levels of LWD density on the physical aquatic habitat of South Fork Obion River, Tennessee, USA. Two secondary objectives in their study were to develop and demonstrate a method for quantifying LWD in a given reach and to relate the quantity of LWD to reach hydraulics. They used a theoretical approach similar to that described by Petryk and Bosmajian (1975) to calculate the effect of LWD on channel roughness, but based their analysis around deriving  $f$  rather than  $n$ . The LWD density in a reach was calculated using the following formula. (Smith and Shields, 1992):



$$DA = \sum_{i=1}^n \frac{A_{Di}}{A} L = (1/L) \sum_{j=1}^4 F_{bj} \sum_{k=1}^3 N_{j,k} F_{wk} \quad (9)$$

where  $DA$  = LWD density ( $m^2$ ),  $n$  = total number of LWD formations in the reach,  $F_{bj}$  = formation type weighting factor for  $j$ th formation type,  $N_{j,k}$  = number of type  $j$  LWD formations in  $k$ th width category, and  $F_{wk}$  = weighting factor based on LWD formation width category. Factors  $F_b$ ,  $N$ ,  $F_w$ ,  $k$  and  $j$  are defined on the LWD survey form devised by Smith and Shields which is presented in the Appendix.

In a channel reach where LWD plays a major role in flow resistance, total resistance can be expressed as (Smith and Shields, 1992):

$$f_t = f_b + f_{debris} \quad (10)$$

where  $f_t$  = total Darcy-Weisbach friction factor,  $f_b$  = boundary friction factor excluding LWD effects, and  $f_{debris}$  = friction factor due to LWD. They then define total head loss over a reach as the sum of a boundary friction loss and a LWD blockage loss as follows:

$$h_L = SL = \frac{[(f_b L/4R) + K_d] V^2}{2g} \quad (11)$$

where  $h_L$  = total head loss (m), and  $K_d$  = dimensionless loss coefficient (dependent upon LWD density). The energy gradient ( $S$ ) is calculated using a total friction factor from the Darcy-Weisbach equation (equation 7).

By substituting equation 7 for  $S$  into equation 11, Smith and Shields (1992) obtained:

$$f_t = f_b + \frac{4RK_d}{L} \quad (12)$$

thus:

$$f_{debris} = \frac{4RK_d}{L} \quad (13)$$

The ratio  $K_d/L$  is then expressed in terms of the LWD density as (Smith and Shields, 1992):

$$K_d / L = DA \quad (14)$$

Smith and Shields (1992) calculated values for  $f_b$  using curves developed by Alam and Kennedy (1969), hydraulic parameters determined from dye tracer tests in the LWD reaches



(which provide direct discharge and velocity estimates (Richards 1982)), and the median bed grain size determined from sieve analysis. Values for  $f_{\text{debris}}$  were then calculated using equations 8, 14 and 15. They then compared computed values of  $f_t$  with values measured using dye tests.

The results of Smith and Shields (1992) study showed a positive correlation between the measured and computed friction factors. However, they recognized that considerable refinement and site-specific adaptation may be required, and that the method does not account for local energy loss because of bends or flow expansion and contraction at bridges, debris dams, or riffles. The method does have a sound theoretical basis, however, and could be usefully employed in future research into the hydraulics effect of LWD. This analysis was further refined by Shields and Gippel (1995) who produced a table of  $f_{\text{debris}}$  values for LWD jams on the Obion River (Tennessee) and the Tumut River (Australia). Their results are used to compare and validate  $f_{\text{debris}}$  values obtained from the flume model (see below).

## **2.4 Flume techniques**

Only two additional papers have been found concerning experimental work on LWD dynamics from a comprehensive literature survey. Young (1991) conducted flume studies to investigate the impact of debris obstruction on flow afflux, while Cherry and Beschta (1986) used a flume with an erodible bed to determine the effect of debris orientation and height above the bed on the depth and extent of bed scour. Neither of these studies made any attempt to scale flume parameters from a field prototype, so results obtained in these studies are useful only to describe the general nature of the processes involved.



### 3 Similarity in Model Scaling

#### 3.1 Basic principles

Model scaling depends upon dimensional analysis whereby the number and complexity of experimental variables which affect a given physical phenomenon are reduced or compacted (White, 1994). There are only four basic dimensions which need be considered in any mechanics problem. These are Mass (M), Length (L), Time (T), and Temperature ( $\theta$ ). This is the MLT $\theta$  system (note that Force (F) sometimes replaces mass, to give the FLT $\theta$  system). Dimensional analysis makes use of the MLT $\theta$  system to create scaling laws which enable one to construct models which faithfully replicate the relative magnitudes of the most important forces that are present in the 'real world' prototype.

Before scaling a model one must consider which parameters are important in that system, i.e. which variables one wishes to measure. This choice introduces a degree of ambiguity into the method, so the engineer must think carefully before selecting a group of variables.

In the case of an open channel flow fluid mechanics problem one is essentially interested in pressure change ( $\Delta p$ ) through a fluid over space and time (Henderson, 1966). If flow is sub-sonic pressure is dependent upon:

$$\Delta p = f(v, L, \rho, \mu, \sigma, g) \quad (15)$$

where  $L$  = a length scale, usually flow depth ( $d$ ) (m),  $\rho$  = fluid density (approx. 1000 kg/m<sup>3</sup> at 20°C; Richards, 1982),  $\mu$  = fluid viscosity (approx. 0.001 m<sup>2</sup>/s at 20°C; Richards, 1982), and  $\sigma$  = fluid surface tension (approx. 0.073 N/m for a water-air interface; Chadwick and Morfett, 1991)

At the core of dimensional analysis is the Buckingham pi ( $\Pi$ ) theorem (see White, 1994; Roberson and Crowe, 1993). This theorem states that for any group of variables selected there are  $n-k$  dimensionless groups that govern the system, where  $n$  is the number of variables and  $k$  is the number of dimensions of importance. If we assume that temperature is not of great importance in the case of a free-surface fluid flow problem,  $k$





= 3 (MLT). In most modeling studies the seven variables listed in equation 15 are usually considered to be of the greatest importance. This suggests that there are  $7 - 3 = 4$  important dimensionless groups in the system. The variables listed in equation 15 have the following MLT dimensions:

Quantity	Symbol	MLT UNITS
Pressure	P	M/LT <sup>2</sup>
Velocity	v	L/T
Length	L	L
Density	$\rho$	M/L <sup>3</sup>
Viscosity	$\mu$	M/LT
Surface Tension	$\sigma$	M/T <sup>2</sup>
Gravity	g	L/T <sup>2</sup>

**Table 1: Dimensions for important fluid mechanics variables**

These variables are then compacted into dimensionless groups according to their dimensional properties. The groups are not derived here as the method is discussed thoroughly elsewhere (see Henderson, 1966, Yalin, 1971, White, 1994). This technique produces the following four dimensionless groups (Roberson and Crowe, 1993):

$$\frac{\Delta p}{\frac{1}{2} \rho v^2} = f\left(\frac{\rho v L}{\mu}, \frac{\rho v^2}{\sigma}, \frac{v}{\sqrt{Lg}}\right) \quad \text{or} \quad C_p = f(\text{Re}, \text{We}, \text{Fr}) \quad (16)$$

where  $C_p$  = Pressure coefficient,  $\text{Re}$  = Reynolds number,  $\text{Fr}$  = Froude Number, and  $\text{We}$  = Weber number. Because pressure distribution in a fluid is an unknown function of  $\text{Re}$ ,  $\text{Fr}$ , and  $\text{We}$ , model studies can only be interpreted accurately if  $\text{Re}$ ,  $\text{Fr}$ , and  $\text{We}$  are severally given the same value in the model as in the prototype.

If a model is to have complete similarity with a prototype there must be geometric similarity (the model looks the same as the prototype), dynamic similarity (model forces are scaled proportionally to the prototype), and kinematic similarity (where flow patterns in the model map onto those of the prototype). This requires that all velocities and accelerations must have the same prototype to model ratio, such that:

$$\frac{(v_a)_p}{(v_a)_m} = \frac{(v_b)_p}{(v_b)_m} \quad (17)$$



where subscripts a = at section 'a', b = at section 'b', p = prototype, and m = model.

### 3.2 Secondary scale ratios

Building a model requires that secondary scale ratios be developed to translate prototype quantities, such as discharge and slope, into corresponding model values. The influence of the Froude number is dominant if the channel has a free surface, so it is of critical importance that Fr has the same value in the model as in the prototype. Thus (Roberson and Crowe, 1993):

$$\frac{Fr_p}{Fr_m} = 1 \quad (18)$$

Having decided that the ratio of the Froude number between model and prototype must equal unity, we can derive a set of scale ratios for MLT as follows.

First, given that g is a universal constant, regardless of scale, the Froude number equation can be rearranged to give a length scale ratio ( $L_r$ ) in terms of flow velocity:

$$\left( \frac{v^2}{gL} \right)_r = \frac{v_r^2}{L_r} = 1 \quad \text{or} \quad L_r = v_r^2 \quad (19)$$

where the subscript r refers to the ratio of prototype to model. Second, the time scale ratio ( $T_r$ ), in order to remain faithful to Froude scaling, must also be deduced as a function of the velocity scale and length scale. Velocity has MLT units of L/T, and the reciprocal is therefore that  $T = Lv^{-1}$ , thus (Yalin, 1971):

$$T_r = L_r v_r^{-1} = L_r^{1/2} \quad (20)$$

Finally, mass is defined by the density of an object or fluid, multiplied by its volume, so mass scale ratio ( $M_r$ ), is equal to (Yalin, 1971):

$$M_r = \rho_r L_r^3 \quad (21)$$

We have now derived a set of scale ratios for MLT based upon unity of the ratio of Froude number between model and prototype, so all other important scale ratios can now be derived similarly using equations 19, 20 and 21. The important scale ratios are shown in Table 2.



Variable Ratio	Symbol	Scale Ratio
Mass	$M_r$	$\rho_r L_r^3$
Length	$L_r$	$L_r$
Time	$T_r$	$L_r v_r^{-1} = L_r^{1/2}$
Velocity	$v_r$	$L_r^{1/2}$
Discharge	$Q_r$	$v_r L_r^2 = L_r^{2.5}$
Force	$F_r$	$M_r L_r T_r^{-2} = \rho_r L_r^3$
Pressure	$p_r$	$F_r L_r^{-2} = \rho_r L_r$

**Table 2: Important scale ratios**

### 3.3 Influence of viscous forces

Scaling hydraulic models is dominated by Froude number scaling (the ratio of gravitational to inertial forces). However, there are other important forces that must be considered.

The Reynolds number is a measure of the viscous to inertial forces in a flow. The only way to maintain the effect of viscous forces is to ensure that both the Froude number and the Reynolds number are the same in the model as in the prototype. This necessarily involves adjusting fluid viscosity in the model but this is very difficult in practice and fresh water is normally the only fluid suitable for modeling. If fluid viscosity is the same in model and prototype and one is scaling according to the Froude principles it becomes evident that:

$$Re_r = \rho_r v_r L_r / \mu_r = L_r^{1.5} \quad (22)$$

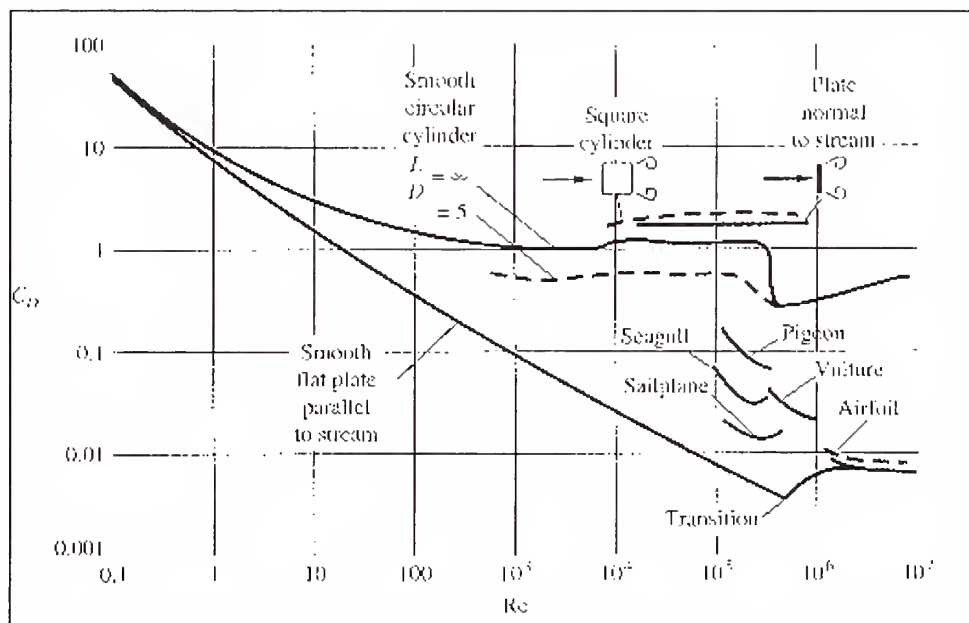
This means that Reynolds numbers will be much smaller in the model than in the prototype.

The importance of maintaining Reynolds number similarity from its relationship with another important dimensionless variable, the drag coefficient ( $C_D$ ) (equation 2) which defines the relationship between drag force and the flow dynamic force.

The drag coefficient of various objects is shown related to Reynolds number in Figure 2. At low Reynolds numbers  $0.1 < Re < 1000$  where flow is laminar, drag on bluff bodies' (cylinders, plates, etc.) increases with  $Re$ . This relationship is controlled by the bodies'



skin-friction, that is, the roughness of the object's surface rather than its overall dimensions. At higher Reynolds numbers where flow is turbulent, skin friction ceases to be important, and it is the overall form of the body which determines the drag coefficient. Form drag remains almost constant with respect to  $Re$  as long as the flow is turbulent. It is this phenomenon that allows the scale modeler to 'cheat' viscous forces, since if only form drag is pertinent in the experimental situation, the drag coefficient will remain roughly similar between model and prototype so long as Reynolds numbers in both imply fully turbulent flow. The important rule in modeling is that  $Re$  should be kept as high as possible in the model situation, but need not match  $Re$  in the field. Several authors give guidelines on the minimum Reynolds number required for accurate modeling. Allen (1947) recommends that the  $Re$  in the model should not be less than 1400.



**Figure 2: The relationship between  $C_D$  and  $Re$  for various objects (after White, 1994).**

The Weber Number (see equation 16) defines the ratio of inertial to surface tension forces acting on a fluid. Surface tension is the tensile force (N/m) acting perpendicular to the surface of a fluid caused by intermolecular forces. Surface tension has a negligible effect upon fluid motion in most rivers because it is a very weak force compared to the





force of gravity. However, where flow depths are small, as in the case of hydraulic models, surface tension may distort the scaling of fluid motion characteristics between prototype and model.

There is no consensus to suggest a single critical Weber number for models to avoid surface tension effects. Studies (see Peakall et al., 1996) suggest that values should exceed 100. White (1994) suggests that the Weber number is important only if it is of the order unity or less. While Novak and Cabelka (1981) suggest three minimum operating conditions to minimise surface tension effects. These are: (1) surface waves on the model should be greater than 0.017m; (2) surface flow velocity should exceed 0.23 m/s to allow gravity waves to develop, and; (3) flow depth in the model should exceed 0.015 m. Noval and Cabelka (1981) also state that the minimum Weber number should be 11. Estimates from model studies range from 2.5 to 17 and from 29 to 160 (see Peakall and Warburton, 1996).

### **3.4 Scaling channel boundary resistance in fixed bed models**

In the previous section we have learned the importance of 'Froude scaling' and the scaling laws which are derived as a consequence. We now need to apply these rules to various types of model construction. First we consider models where one is simply interested in replicating the forces and flow structure of a prototype. Second we discuss the far more complex problem of scaling deformable boundary models and similarity of sediment transport, as this leads us towards a solution for the experimental problem which is considered in this research.

It is, of course, evident that one must maintain similarity of boundary resistance between model and prototype channels. Henderson (1966) uses the Manning formula to express the ratio of boundary flow resistance between model and prototype:

$$v_r = \frac{R_r^{2/3} S_r^{1/2}}{n_r} \quad (23)$$

where  $v_r$  = velocity ratio,  $R_r$  = hydraulic radius ratio,  $S_r$  = energy gradient ratio, and  $n_r$  = Manning's  $n$  ratio.



If we intend to build a model which has geometric similarity it follows that  $S_r=1$  and  $R_r=L_r$ . So, rearranging equation 23 with respect to  $n_r$  and bearing in mind the relation developed in equation 20 we find that:

$$n_r = \frac{L_r^{2/3}}{L_r^{1/2}} = L_r^{1/6} \quad (24)$$

This condition must be met if dynamic similarity is to be achieved. The relation  $n_r = L_r^{1/6}$  is very similar in nature to Strickler's definition of absolute  $n$  which he derived from field evidence in gravel-bed rivers (Richards, 1982), where:

$$n = 0.0151 D_{50}^{1/6} \quad (25)$$

This similarity lead Einstein and Chien (1954) to the conclusion that  $n$  as defined by equation 25 for a model situation is directly and geometrically proportional to  $n$  as empirically measured in the prototype. In other words,  $n_r$  is dependent upon boundary geometric similarity, regardless of whether friction is predominantly caused by skin roughness (as will be the case in the model) or form roughness (as will be the case in the prototype). We can therefore combine equations 24 and 25 to give:

$$n_r \approx D_{50r}^{1/6} \quad (26)$$

Achieving similarity of  $n$  is not quite so simple, however, because  $n$  is also a function of Reynolds number which will be proportionally much smaller in the model as compared to the prototype. One could solve this problem by proportionally reducing surface roughness in the model, but this is often physically impossible if the prototype surface in question is already smooth. The conclusion is that turbulence must be made as high as possible in the model situation in order to preserve boundary roughness scaling. And it is usually impossible to change model fluid viscosity, we are left with only one other variable in the Reynolds number equation which we can adjust to keep  $Re$  as high as possible:  $L$  or flow depth.

### 3.5 Scale distortion



Why distort model geometric scaling? For three important reasons: (1) to solve the problem of low model Reynolds numbers, as greater flow depths in a model will ensure that the flow is fully turbulent; (2) because pure geometric scaling may result in model flow depths that are too small to enable accurate instrumentation, and; (3) because if depth is too small surface tension effects may distort the scaling of flow processes between model and prototype.

If a model is distorted,  $L_r$  must be split into two variables;  $Y_r$ , a vertical scale, and  $X_r$ , a horizontal scale. The Froude scaling relationship now takes the form (Henderson, 1966):

$$v_r = Y_r^{1/2} \quad (27)$$

because it is vertical rather than horizontal distance which determines the effect of gravity on velocity. However, velocity acts in essentially a horizontal direction, so the time scale becomes:

$$T_r = X_r / v_r = X_r / Y_r^{1/2} \quad (28)$$

discharge scale becomes:

$$Q_r = v_r X_r Y_r = X_r Y_r^{3/2} \quad (29)$$

slope scale becomes:

$$S_r = Y_r / X_r \quad (30)$$

and force scale becomes:

$$F_r = \rho_r X_r^2 Y_r / X_r T_r^{-2} = \rho_r X_r^2 Y_r \quad (31)$$

Also, substituting equation 30 into equation 23, we find that:

$$v_r = \frac{R_r^{2/3} Y_r^{1/2}}{n_r X_r^{1/2}} \quad (32)$$

Which, when combined with equation 27 yields:

$$n_r = \frac{R_r^{2/3}}{X_r^{1/2}} \quad (33)$$

A consequence of equation 33 is that  $n_r$  will usually be less than unity, so that  $n$  in the model is by necessity of the scale distortion greater than that in the prototype, which therefore reduces the effect of low Reynolds numbers in the model. Correct model  $n$  values are usually determined on a trial and error basis by adjusting roughness until the



stage-discharge relationship in the model is similar to that of the prototype. It is also worth noting that in some instances  $S_r$  is made greater than  $Y_r/X_r$  in moveable-bed models in order to assist sediment movement: this practice is known as ‘tilting’ the model (Henderson, 1966).

### 3.6 Moveable bed models

Moveable bed models are more complex to scale than fixed bed models because parameters such as sediment density and grain size must be considered. The scale relationships discussed in the previous section must also be maintained. Moveable bed models were built on a trial and error basis at one time (Henderson, 1966). Explicit design methods currently available (Yalin, 1971; Einstein and Chien, 1954; Blench, 1955) use the Shields and Particle Reynolds parameters as a basis to model sediment transport. The rationale for this is that the Shields and Particle Reynolds numbers are dimensionless parameters that can be utilized for scaling in the same manner as the Froude and Reynolds numbers.

The method proposed by Einstein and Chien (1954) is used herein. The method assumes that the shape of the bed, and sediment transport properties can be preserved between model and prototype by exactly matching parameters of the Shields entrainment function over the range of design discharges. Figure 3 shows the Shields entrainment function. The Shields function is defined by the Shields parameter ( $\theta_*$ ), where:

$$\theta_* = \frac{\tau_0}{(\gamma_s - \gamma)D} \quad (34)$$

where,  $\gamma_s$  = bulk unit weight of sediment =  $\rho_s$  (sediment density, kg/m<sup>3</sup>) x g,  $\gamma$  = bulk unit weight of water =  $\rho$  x g (approx. 9810 N/m<sup>3</sup>),  $D$  = representative grain size (usually taken to be  $D_{50}$ ), and  $\tau_0$  = boundary shear stress, defined as:

$$\tau_0 = \gamma RS \quad (35)$$

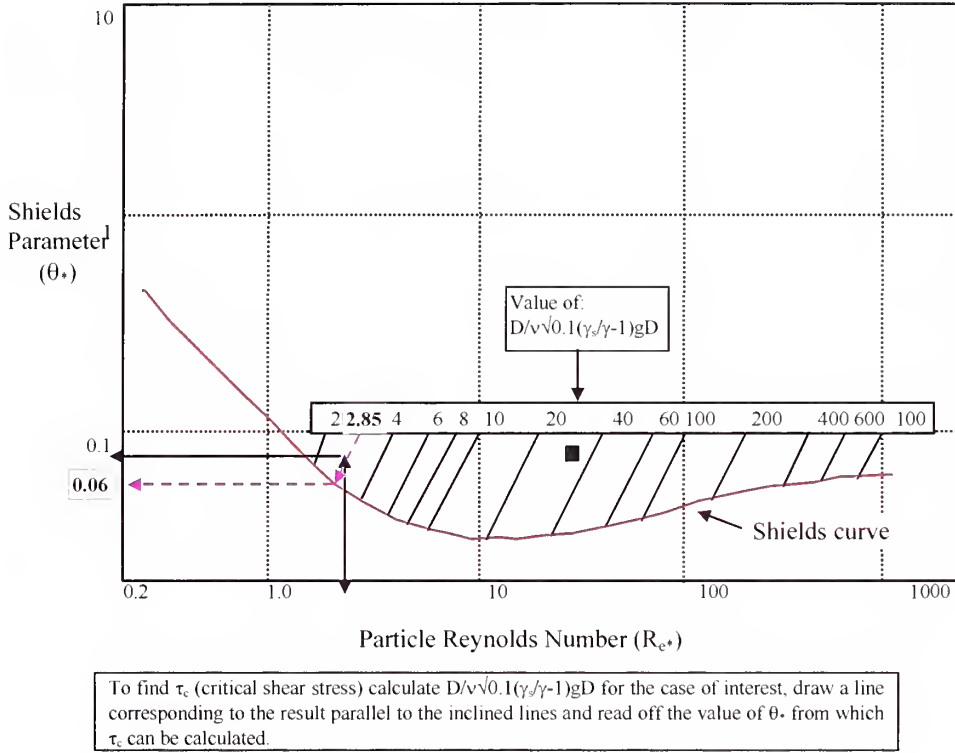
and the Particle Reynolds number ( $R_{e*}$ ), where:

$$R_{e*} = \frac{U_* D}{\nu} \quad (36)$$





where  $U_* = \text{shear velocity} = \sqrt{\tau_0 / \rho}$ . The aim is to make  $\theta_{*p} / \theta_{*m} = 1$  and  $R_{e* p} / R_{e* m} = 1$  in order to achieve similarity of sediment transport.



**Figure 3: The Shields entrainment function (modified from Vanoni, 1966)**

If bed configuration is the same in the model as in the prototype, boundary roughness ( $k$ ) will also be in the same ratio ( $k = 1/30 \times D_{65}$ , where,  $D_{65}$  = Nikuradse sand roughness; Richards, 1982). It therefore follows that  $n$  will be in the same ratio, so we can substitute equation 26 into 33 to give:

$$D_{50r}^{1/6} = \frac{R_r^{2/3}}{X_r^{1/2}} \quad (37)$$

that solves Manning and Froude scaling for a mobile boundary scale distorted model.

A second consequence of boundary roughness being in the same ratio as model and prototype is that the ratio of grain resistance ( $R'$ ) to form resistance ( $R''$ ) will equal



unity. Thus, boundary shear stress will also be proportional between model and prototype, so:

$$\tau_{0r} = \gamma_r R_r S_r = \gamma_r R_r Y_r / X_r \quad (38)$$

The development of equations 37 and 38 mean that equations 34 and 36 can now be derived in terms of scale ratios. Thus to scale sediment transport correctly we require:

$$\theta_{*r} = \frac{R_r Y_r}{\gamma_{sr} X_r D_r} = 1 \quad (39)$$

and:

$$Re_{*r} = \frac{R_r Y_r D_r^2}{X_r \nu_r^2} = 1 \quad (40)$$

Assuming that  $\nu_r = 1$  between model and prototype (fresh water in both), means that there are four independent variables ( $Y_r$ ,  $X_r$ ,  $D_r$ , and  $\alpha_r$ ) in equations 37, 39 and 40, which have to be solved simultaneously in order to achieve Froude scaling for a mobile boundary model. The designer is therefore free to choose one of the four independent variable scale ratios. It is also worth noting that the model must have scale distortion (i.e.  $X_r \neq Y_r$ ) in order to solve this set of equations. This system offers an excellent analytical solution to mobile boundary scaling, but it is somewhat inflexible and so requires that the designer have unlimited flume construction options and specialized physical materials at his disposal. Scaling was pursued in the flume model using the Manning-Froude equation (37) and the Shields-Particle Reynolds equations (39 and 40).



#### 4 Abiaca Creek Scaling Method

The first step in creating a physical model was to select a representative reach from the study sites as a prototype for the model. The prototype reach selected was in Abiaca Creek in Northern Mississippi.

The appropriate channel dimensions were then determined by assuming that the most important discharge in the prototype river, in terms of affecting channel geomorphology (the dominant discharge), was the two-year flood ( $Q_2$ ).  $Q_2$  is often considered to be the dominant geomorphic discharge (Summerfield, 1991), and the rationale for this assumption is discussed in many fluvial geomorphology texts (Richards, 1982, Knighton, 1984).

The necessary prototype dimensions were obtained from survey studies conducted by Watson et. al. (1993) and are listed in Table 3.

Variable	Symbol	Value
Two Year Discharge	$Q_2$	48.1 m <sup>3</sup> /s
Average Width	w	17.9 m
Average Depth	d	1.9 m
Hydraulic Radius	R	1.57 m
Width/Depth Ratio	w/d	10
Average Bed-Slope	S	0.0011
Estimated Manning's n	n	0.032
Sediment D <sub>50</sub>	D <sub>50</sub>	0.25 mm

**Table 3: Hydraulic variables for the prototype reach in Abiaca Creek at  $Q_2$  discharge**

The flume used to conduct the experimental study had an overall channel width of 0.63 m, a depth of 0.61 m, and a total length of 10.0 m. Slope on this apparatus was adjustable by means of a power-driven hydraulic jack. Flow entrance conditions were calmed by passing the water vertically through a gravel filled feeder tank into the flume.

As discussed above, the model had to have mobile bed and banks and be fully Froude scaled. However it was also necessary for the model channel boundary to be at the



threshold of motion at the  $Q_2$  discharge so that geomorphic change only occurred with the introduction of simulated LWD elements. In this way, the impact of LWD on channel geomorphology could therefore be isolated from other channel adjustment process. The prototype channel boundary is well above the threshold of motion at the  $Q_2$  discharge however, so it was not possible or desirable to achieve scaling similarity for sediment transport between the model and prototype. Scaling proceeded using the methodology developed by Einstein and Chen 1954) as discussed above.

Froude and Manning scaling is achieved by selecting only one of the possible hydraulic variables. Given that the flume had a width constraint of 0.61 m it was decided to fix the initial flume width at 0.3 m to allow for lateral adjustment during test runs. All other model scale relationships had now to be developed to solve equation 39, the Froude-Manning scaling law. We therefore required  $X_r$ :

$$X_r = X_p / X_m = 17.9 / 0.3 = 59.667$$

and  $Y_r$ . If the model had no scale distortion  $Y_r = X_r$ , so:

$$Y_m = Y_p / Y_r = 1.9 / 59.667 = 0.03 \text{ m}$$

The flume depth would therefore have been 0.03 m. However, it was considered that this depth was too small as fully turbulent flow might not have developed and surface tension effects could well have been significant. The solution was therefore to give up true geometric scaling by distorting the vertical scale. This practice is quite legitimate and was an absolute necessity for equations, 37, 39 and 40 to be solved simultaneously (Henderson, 1966). We doubled the geometrically scaled flume depth to 0.07 m. Thus:

$$Y_r = Y_p / Y_m = 1.9 / 0.07 = 27.142$$

Lastly we require  $R_r$ , which must be derived from  $Y_r$  and  $X_r$ . Hydraulic radius ( $R$ ) is defined as:

$$R = A / P \tag{41}$$

where  $A = w \times d$ , and  $P = \text{wetted perimeter} = 2d + w$ . So the hydraulic radius ratio is determined as:

$$R_r = Y_r \times X_r / [(2 \times Y_r) + X_r] \tag{42}$$

$$R_r = 27.142 \times 59.667 / [(2 \times 27.142) + 59.667] = 14.21$$

Model hydraulic radius is therefore:





$$R_m = R_p / R_r = 1.57 / 14.21 = 0.110 \text{ m}$$

$R_r$  and  $X_r$  can now be substituted into equation 22 to yield  $D_r$ :

$$D_r^{1/6} = 14.21^{2/3} / 59.667^{1/2} = 0.192$$

The required boundary grain size in the model was therefore:

$$D_m = D_p / D_r = 0.00025 / 0.192 = 1.3 \text{ mm}$$

Material constraints at the laboratory however meant that the closest grain size available was 0.8-mm quartz sand, which had a density of 2620 kg/m<sup>3</sup>. The model boundary roughness was therefore slightly lower than that required for pure Froude-Manning scaling, the consequence being that the model channel had slightly less boundary resistance than the prototype.

Now that  $X_r$  and  $Y_r$  were calculated it was possible to determine the required flume slope,  $S_r$ :

$$S_r = Y_r / X_r = 27.142 / 59.667 = 0.45$$

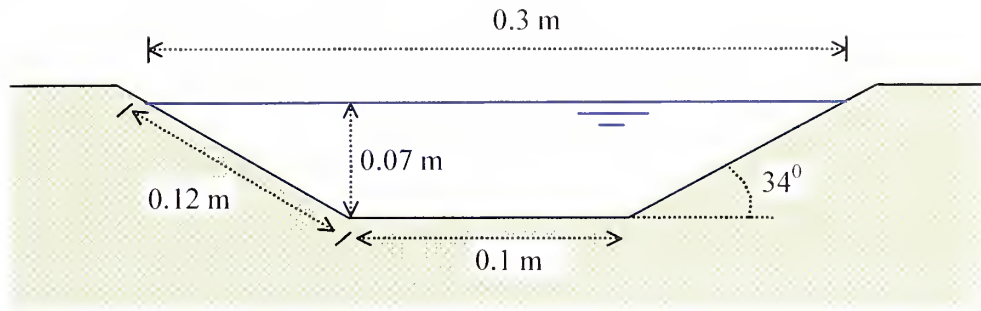
Thus:

$$S_m = S_p / S_r = 0.0011 / 0.45 = 0.0024 \text{ m/m}$$

At this point the model dimensions were scaled as accurately as physical constraints would allow according to Froude-Manning scaling laws for a depth-distorted model.

Given these initial dimensions, tests were conducted to determine what flume geometry was practically possible, given that the channel boundary was to be molded from 0.8-mm sand. Through trial and error tests it was found that the stable angle of repose for the saturated sand was 34° degrees. The channel banks could therefore not be made near vertical, as was the case in the prototype. The closest approximation to the prototype for the flume geometry as required by the scaling parameters that had stable banks, is shown in Figure 4.





**Figure 4: Cross section of flume channel (dimensions in meters).**

This channel has the following hydraulic dimensions: (1) cross-sectional area =  $0.014 \text{ m}^2$ , (2) wetted perimeter =  $0.35 \text{ m}$ , (3) hydraulic radius =  $0.04 \text{ m}$ .

It should be noted that the measured hydraulic radius for the flume ( $0.04 \text{ m}$ ) is smaller than the hydraulic radius determined through the scaling technique ( $0.11 \text{ m}$ ). This difference is due to the fact that the channel had to have sloping, rather than vertical banks. This difference, however, does not significantly compromise the initial scaling procedure. Indeed, the discrepancy between the actual and scale-derived flume  $R$  even helped to maintain parity of effective boundary roughness between flume and prototype by compensating for the mismatch between the boundary grain size required through scaling and the smaller grain size which had to be used.

The model was not complete at this stage, however, because we required that the channel boundary be at the threshold of motion. Mobile boundary scaling techniques now had to be employed. Adopting the rational scaling method proposed by Einstein and Chien (1954), solutions had to be found to equations 41 and 42 for the model-prototype dimensions. First, scale relationships had to be determined for the fluid kinematic viscosity ratio ( $\nu_r$ ) and sediment density ratio ( $\gamma_r$ ) in order to solve these equations.

Given that fresh water had to be used in the model  $\nu_r$  was assumed to equal one:

$$\nu_r = \nu_p / \nu_m = 1 \times 10^{-6} / 1 \times 10^{-6} = 1$$



sediment density of bed material in the prototype is roughly  $2620 \text{ kg/m}^3$  (Watson et al., 1993), which is the same as that of the sand used in the model, so  $\alpha_r$  was also assumed to equal one:

$$\gamma_r = \gamma_p / \gamma_m = 2620 \times 9.81 / 2620 \times 9.81 = 1$$

The necessary scale ratios were all derived so it was now possible to solve the Shields and Particle Reynolds scaling functions. All scale ratios and physical dimensions for the flume model are shown in Table 4.

Scaling factor	Symbol	Scaling value	Comparable dimension	Flume value
Horizontal	$X_r$	59.667	Flow width	0.300 m
Vertical	$Y_r$	27.142	Flow depth	0.070 m
Hydraulic radius	$R_r$	14.212	Hydraulic radius	0.04 m
Slope	$S_r$	0.45	Water surface slope	0.0024
Kinematic viscosity	$\nu_r$	1	Kinematic viscosity	$1 \times 10^{-6} \text{ m}^2/\text{s}$
Bulk sed. density	$\gamma_r$	1	Bulk sed. weight	$25702 \text{ N/m}^3$
Sediment grain size	$D_r$	0.192	Sediment $D_{50}$	1.3 mm

**Table 4: Scaling factor values and main flume dimensions determined by Froude-Manning scaling**

The threshold boundary condition desired for the flume model, the  $Q_2$  discharge, was not similar to the boundary condition in the prototype reach at  $Q_2$  because as significant sediment transport occurs in Abiaca Creek even at flows less than  $Q_2$ . Equations 39 and 40 could not therefore have products of unity to fulfil the requirements of the model. It is instructive however to calculate the Shields parameter and Particle Reynolds parameter ratios for the scale ratios presented in Table 4 for demonstration.

Remember that  $\theta_{*r} = R_r Y_r / \gamma_r X_r D_r$ . Thus:

$$\theta_{*r} = (14.212 \times 27.142) / (1 \times 59.667 \times 0.192) = 33.667$$

And that  $Re_{*r} = R_r Y_r D_r^2 / X_r \nu_r^2$ . Thus:

$$Re_{*r} = (14.212 \times 27.142 \times 0.192^2) / (59.667 \times 1^2) = 0.238$$

We see to restore  $\theta_{*r}$  to unity without distorting the  $R_r$ ,  $X_r$ ,  $Y_r$  and  $D_r$  determined by Froude scaling,  $\gamma_r$  must be made greater than one by reducing the model sediment density.



To restore  $Re_{*r}$  to unity,  $v_r$  must be made less than one by increasing the model fluid viscosity. These adjustments were not possible given the laboratory equipment available.

The hydraulic conditions at the threshold of motion must be determined. First, we had to determine the Shields and Particle Reynolds numbers for the hydraulic variables defined in Table 4, and find where the two values intersected on the Shields entrainment function diagram (see Figure 3). These parameters were calculated as follows (note that we have used the measured channel hydraulic radius of 0.04 m, rather than the theoretical value determined by scaling (0.11 m) as the former value represents the true model hydraulic condition). The Shields parameter  $= \theta_* = \tau_0 / (\gamma_s - \gamma) D_{50}$ , where,  $\tau_0 = \gamma R S$ . Thus:

$$\theta_{*m} = 9810 \times 0.04 \times 0.0024 / [(25702 - 9810) \times 0.0008] = 0.073$$

and the Particle Reynolds parameter  $= Re_* = U_* D_{50} / \nu$ , where,  $U_* = \sqrt{\tau_0 / \rho_w}$ . Thus:

$$Re_{*m} = \sqrt{(9810 \times 0.04 \times 0.0024) / 1000} \times 0.0008 / 1 \times 10^{-6} = 24.55$$

Plotting these values on the Shields entrainment function (Figure 3), the intersect is above the critical curve (square marker) so the model did not have a threshold boundary condition for the pure Froude-Manning scaled variables. We therefore employed the technique of ‘tilting’ the model by adjusting the prescribed slope so that the Shields parameter was reduced to the critical value ( $\theta_{*c}$ ). The model therefore had a slope condition where  $S_r \neq Y_r / X_r$ .

The slope required for a threshold boundary condition was determined by substituting an appropriate Shields value into equation 36 and solving for the slope. The threshold curve in Figure 3 can be used to visually determine a critical Shields value for a known particle Reynolds number. However, methods developed by Bogardi, (see Henderson, 1966), and Vanoni (1966) more accurately determine  $\theta_{*c}$  for a given boundary roughness based upon empirically derived equations. In Vanoni’s method  $\theta_{*c}$  is determined by calculating a value for the following equation:

$$\frac{D_{50}}{\nu} \sqrt{0.1 \left( \frac{\gamma_s}{\gamma} - 1 \right)} g D_{50} \quad (43)$$





A line is then drawn corresponding to that value parallel to the inclined lines on Figure 3, down to the threshold curve, and then horizontally, parallel to the x axis, to intersect with  $\theta_{*c}$  on the y axis. We used this procedure to determine  $\theta_{*c}$  for the model. Substituting model values into equation 43 gives:

$$0.0008/1 \times 10^{-6} \times \sqrt{0.1 (25702 / 9810) - 1} \times 9.81 \times 0.0008 = 2.85$$

Drawing a line corresponding to this value parallel to the inclined lines on Figure 3 and reading off the value horizontally yielded a critical Shields parameter  $\theta_{*c}$  of 0.060. This value was then substituted into the Shields equation to determine the critical slope for the model:

$$0.060 = 9810 \times 0.04 \times S_m / (25702 - 9810) \times 0.0008$$

which yields:

$$S_m = 0.0019$$

It was therefore necessary to initially relax the flume slope from the Froude scaled value of 0.0024 down to 0.0019 in order to guarantee a critical threshold boundary condition.

The flume channel was then constructed using the dimensions shown in Figure 4, with a bed slope of 0.0019. A discharge was then run through the channel and increased incrementally until flow depth reached 0.07 m. The flume was then left to stabilize for several hours to make sure that sediment transport did not occur. No transport was observed so slope was increased slowly to determine where the critical condition lay. Through trial and error it was discovered that the water surface slope required for the threshold of particle motion was actually 0.0022, a value close to the slope of 0.0024 that was initially required for scaling similarity. Consequently, the channel slope was set to 0.0022 giving a pre-test channel that closely achieved both Froude-Manning scaling and a threshold boundary condition.

At the bankfull stage, with channel slope set to 0.0022, model discharge ( $Q_m$ ) measured at the flume outlet was  $0.0033 \text{ m}^3/\text{s}$ .

This measured value can be compared with the model discharge predicted by the scaling laws ( $Q_{m(s)}$ ) to provide a check on the calculations. Remember that  $Q_r = X_r Y_r^{1.5}$  (equation 29). Now this equation assumes continuity of flow in the manner:



$$Q = v \times A \quad (44)$$

where  $A = w \times d = X \times Y$ .

However, the channel cross section in the model is not rectangular, so  $A \neq X \times Y$ . Cross-sectional area in the flume is 0.014 m, so it is a simple matter to calculate a critical depth ( $Y_c$ ) to satisfy equation 44.

$$Y_c = A / X = 0.014 / 0.3 = 0.046 \text{ m}$$

Now calculating  $Y_r$  using  $Y_c$  we find:

$$Y_r = 1.9 / 0.046 = 41.30.$$

$Q_r$  can now be calculated correctly:

$$Q_r = 59.667 \times 41.30^{1.5} = 15836.5$$

Model discharge as determined by scaling ( $Q_{m(s)}$ ) is therefore:

$$Q_{m(s)} = Q_p / Q_r = 48.1 / 15836.5 = 0.0030 \text{ m}^3/\text{s}$$

Discharge derived by scaling ( $0.0030 \text{ m}^3/\text{s}$ ) was therefore in good agreement with the discharge measured at the flume outlet ( $0.0033 \text{ m}^3/\text{s}$ ), and we were therefore satisfied that all variables had been calculated accurately.

Finally, depth averaged velocity was derived for the flume ( $v_m$ ) using equation 44. This yields:

$$v_m = Q / A = 0.0033 / 0.014 = 0.24 \text{ m/s}.$$

A comparison of Froude values in the prototype channel and model channel should yield the following relationship if scaling is correct:  $Fr_p / Fr_m = 1$  (equation 20). Using the derived flow velocity of 0.24 m/s the Froude number for the model was:

$$Fr_m = v / \sqrt{gd} = 0.24 / \sqrt{9.81 \times 0.07} = 0.29$$

While the Froude number for the 2-year discharge event in Abiaca Creek is:

$$Fr_p = 1.4 / \sqrt{9.81 \times 1.9} = 0.32$$

Thus:

$$Fr_p / Fr_m = 0.32 / 0.29 = 1.10$$

The model flow conditions were therefore very close to the ideal condition for unity in Froude scaling.



Reynolds number for the flume was:

$$Re_m = vd / \nu = 0.24 \times 0.07 / 1 \times 10^{-6} = 16800$$

while Reynolds number for the 2-year discharge event in Abiaca Creek is:

$$Re_p = 1.4 \times 1.9 / 1 \times 10^{-6} = 2660000$$

There is therefore a great difference in the model and prototype Reynolds numbers. However, because the model Reynolds number is high enough to ensure fully turbulent flow (Allen (1947) suggests model values should exceed 1400), the difference in absolute values is not critical. This is because drag coefficients on immersed bodies remain almost identical for the entire range of flow Reynolds numbers that signify a fully turbulent flow (refer to Figure 2). The flume model was considered adequately scaled according to the two most important hydraulic dimensionless parameters.

One further dimensionless coefficient, the Weber number, had also to be determined for the flume however in order to ensure that surface tension effects were not significant. Recall that the Weber number =  $We = v^2 \rho_w d / \sigma$ . Thus:

$$We_m = 0.24^2 \times 1000 \times 0.07 / 0.073 = 55.23$$

This value lie in the middle of the range quoted for other hydraulic models, while the criteria suggested by Novak and Cabelka (1981) are all exceeded by the model (although length of surface waves were unknown). So, despite some confusion in the literature concerning a precise limiting Weber number, we were satisfied that the model at least met the minimum criteria to ensure that fluid motion would was not significantly affected by surface tension effects during the test runs. Table 5 shows a comparison of prototype and model variable dimensions. Figure 5 shows a flow diagram of the scaling procedure used to construct the model.

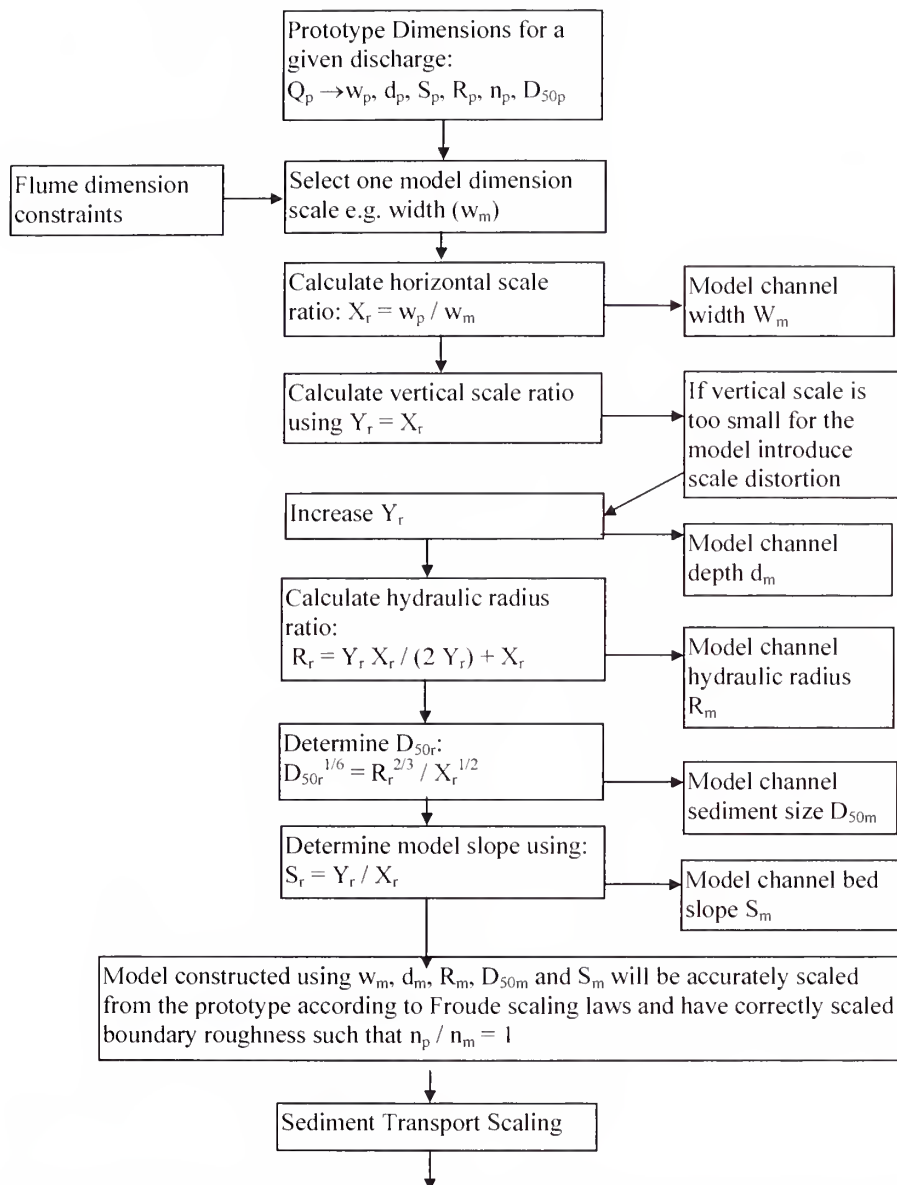


Variable	Symbol	Units	Model	Prototype
Channel width	w	m	0.30	17.90
Reach length	L	m	1.00	65.00
Flow depth	d	m	0.07	1.90
Bed slope	S		0.0022	0.0011
Hydraulic radius	R	m	0.04	1.57
Cross-sectional area	A	m <sup>2</sup>	0.014	34.00
Wetted perimeter	P	m	0.35	21.70
Bankfull discharge	$Q_b / Q_2$	m <sup>3</sup> /s	0.0033	48.10
Derived mean flow velocity at $Q_b$	v	m/s	0.24	1.40
Representative grain size	$D_{50}$	mm	0.8	0.25
Sediment density	$\rho_s$	kg/m <sup>3</sup>	2650.0	2620.0
Width-to-depth ratio	w/d	-	4.20	10.00
Particle Reynolds number at $Q_b$	$Re^*$	-	2.32	3.25
Shields Parameter at $Q_b$	$\theta^*$	-	0.060	1.27
Shear velocity at $Q_b$	$U^*$	-	0.029	0.130
Manning's n	n	-	0.023	0.032
Important Dimensionless Coefficients				
Froude number	Fr	-	0.29	0.32
Reynolds number	Re	-	16800	2660000
Weber number	We	-	55.23	51013.70

**Table 5: Comparison of model and prototype channel variables**

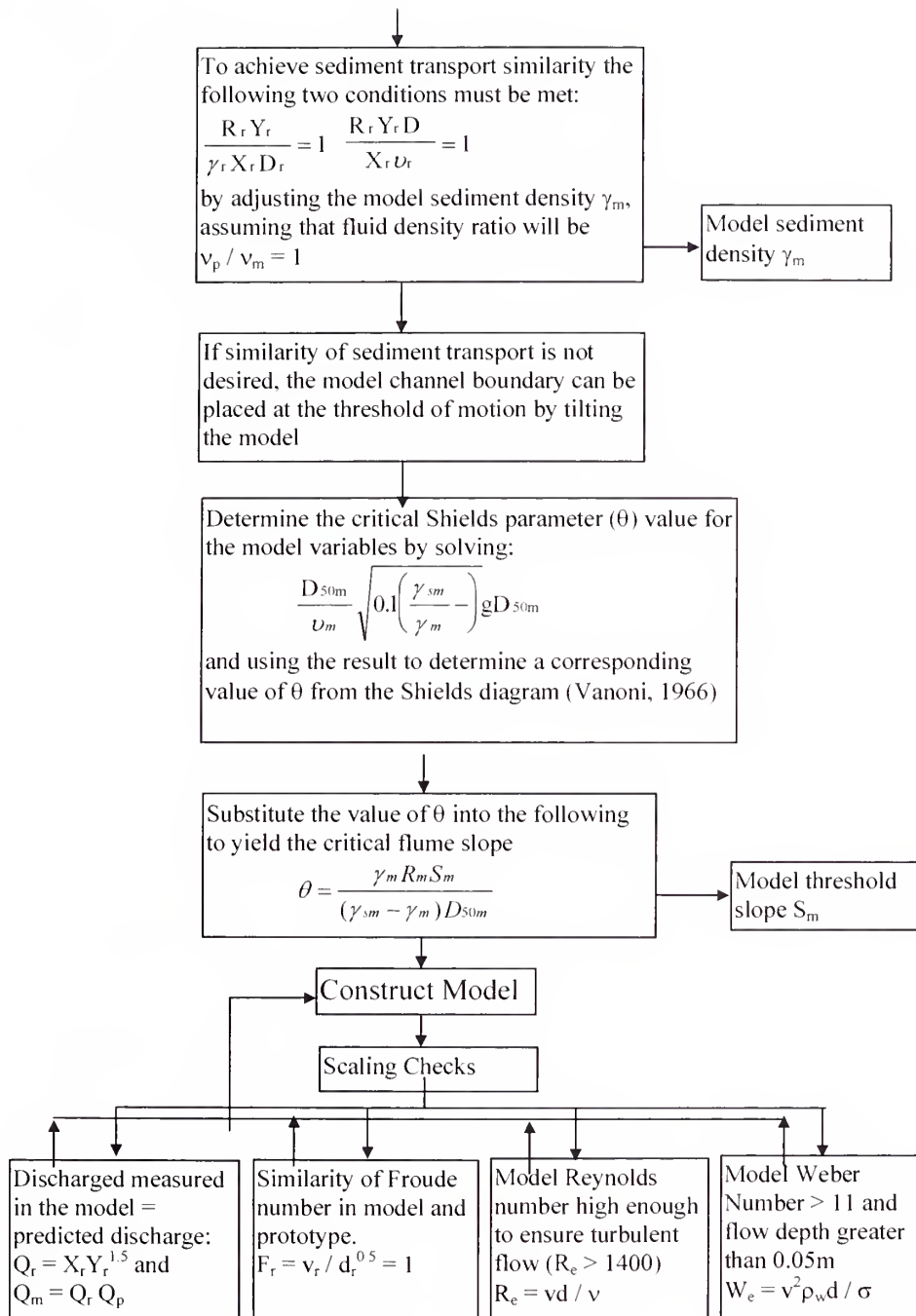






**Figure 5: Flow diagram of procedure for creating a Froude scaled mobile boundary flume model from a prototype river**





**Figure 5: Continued**



## 5 Flume Design and Construction

The intention of the flume analysis was to test the geomorphic and hydraulic impact of the four distinct jam types (Underflow, Dam, Deflector, and Flow Parallel) which were identified in the field and conceptualized in the Debris Jam Classification Model (refer to Wallerstein et al., 1997). Two important simplifications were made in the flume model to ensure that results would be repeatable. First, rather than creating jams made from a number of complex elements, single cylindrical elements were used representing the 'key' debris element in each jam type. Second, rather than using one average representative key debris (tree) height and varying the flume channel width to simulate the different debris length to channel width ratios suggested in the Debris Jam Classification Model, the reverse was done. Flume channel width was fixed and debris element lengths were changed to simulate varying debris length to channel width ratios. This compromise was made to maintain scale similarity in the flume. Table 6 details the relative and absolute proportions of the LWD elements used in the flume.

Each element was positioned in the channel to simulate the natural location of LWD if it were to fall perpendicular to the flow in the prototype channel. Figure 6 shows a schematic diagram of the element positions in the flume.

Debris Jam Classification Type	Average debris lengths as a proportion of channel width	LWD element lengths in flume (m)	Average LWD diameter as a proportion of flow depth	LWD element diameter in flume (m)
Underflow	1.00	0.30	0.27	0.019
Dam	0.50	0.15	0.27	0.019
Deflector	0.33	0.10	0.27	0.019
Parallel	0.23	0.07	0.27	0.019

**Table 6: LWD proportions**

The 0.3 element, representing underflow type LWD, almost spans the channel at the bankful level. The 0.15 m, 0.1 m and 0.07 m elements were positioned to simulate the hypothetical case of LWD falling from the left bank into the channel. It must be noted that the elements were not touching the channel boundary at the start of each run.



The flume apparatus is displayed in Figure 7. The channel was created by pre-wetting the sand and then cutting the cross-sectional form into the length of the flume using a scraper plate, machined to the dimensions given in Figure 4, and attached to a carriage mounted on top of the flume. Excess sand was carefully removed and any irregularities in the channel carefully smoothed. Plate 1 shows the model channel and scraper plate prior to running.

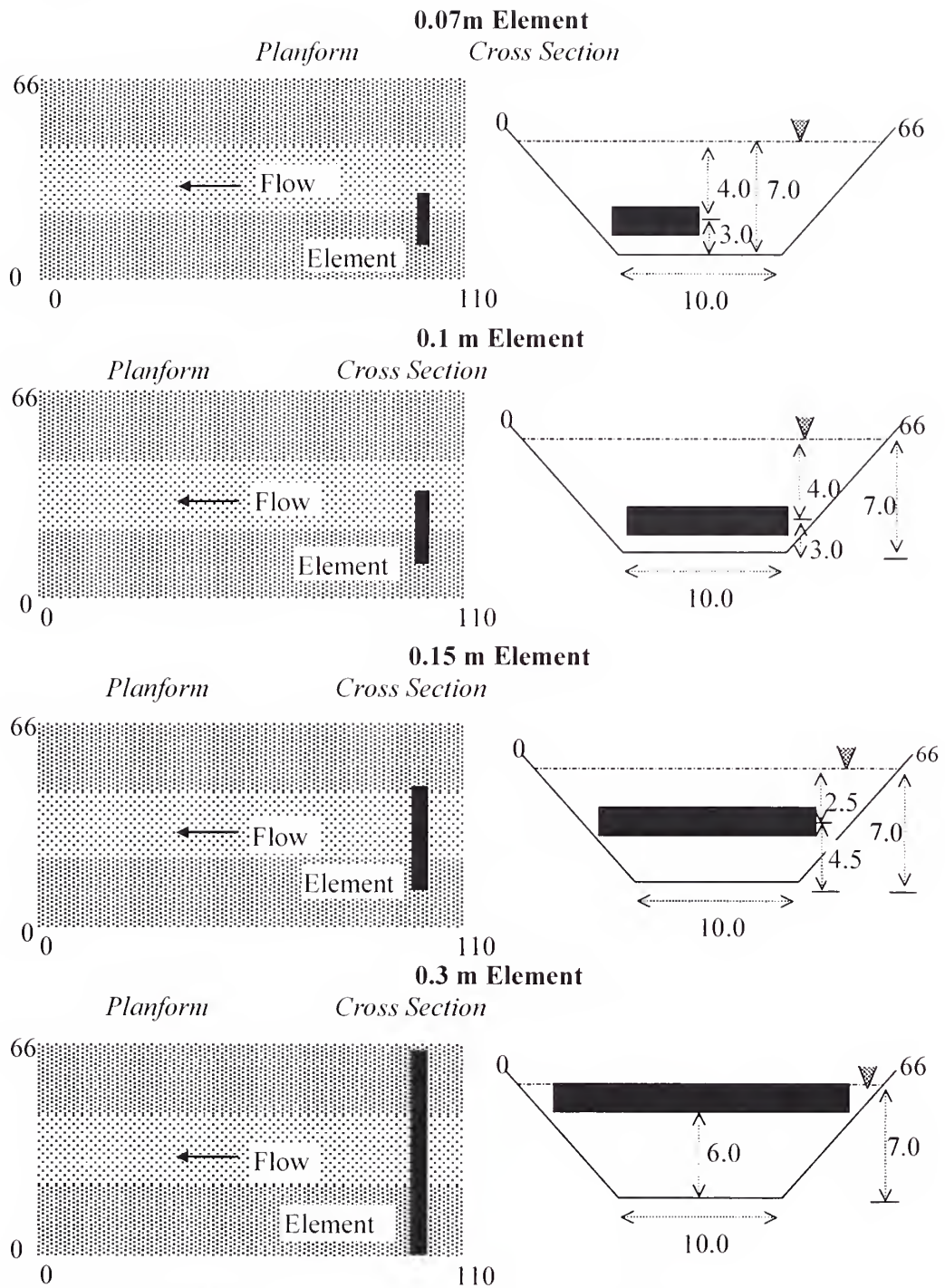
Slope was adjusted to the correct level using a calibrated jack attached to the upstream end of the flume. An adjustable recirculating pump was used to drive the flow through the flume, and discharge was calculated using a v-notch weir. The weir was set into the outlet of a collecting tank located beneath the flume outlet.

It was necessary to install a rectangular weir plate at the flume outlet which could be raised from the bed upwards in order to prevent the flow, accelerating over the outlet, from increasing the total head in the lower end of the flume. This discontinuity in the energy gradient caused limited bed load sediment transport towards the end of the flume until the problem was rectified using the weir plate. Plate 2 shows the undisturbed water surface in the channel, upstream of the test section.

Debris elements were made from cylindrical aluminum stock, cut to appropriate lengths. A mechanical strain gauge was devised to calculate the dynamic pressure force on the elements during test runs. This apparatus is shown in Figure 8.



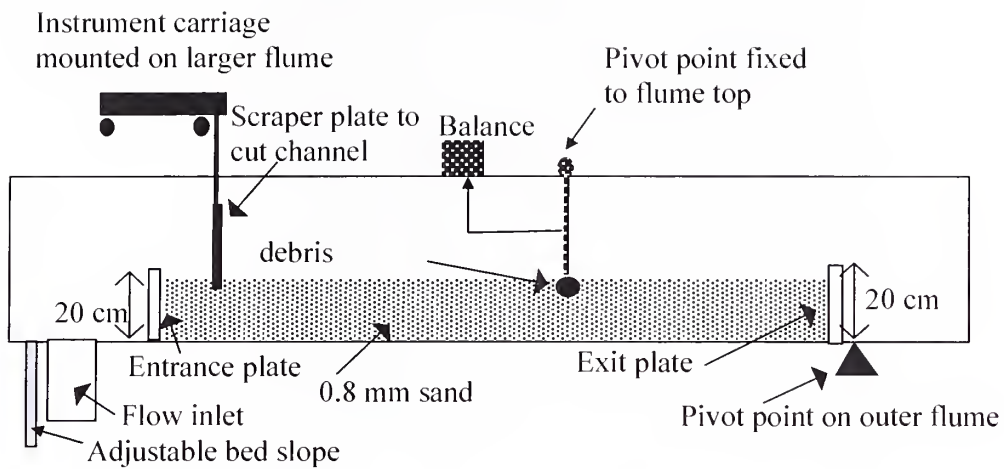




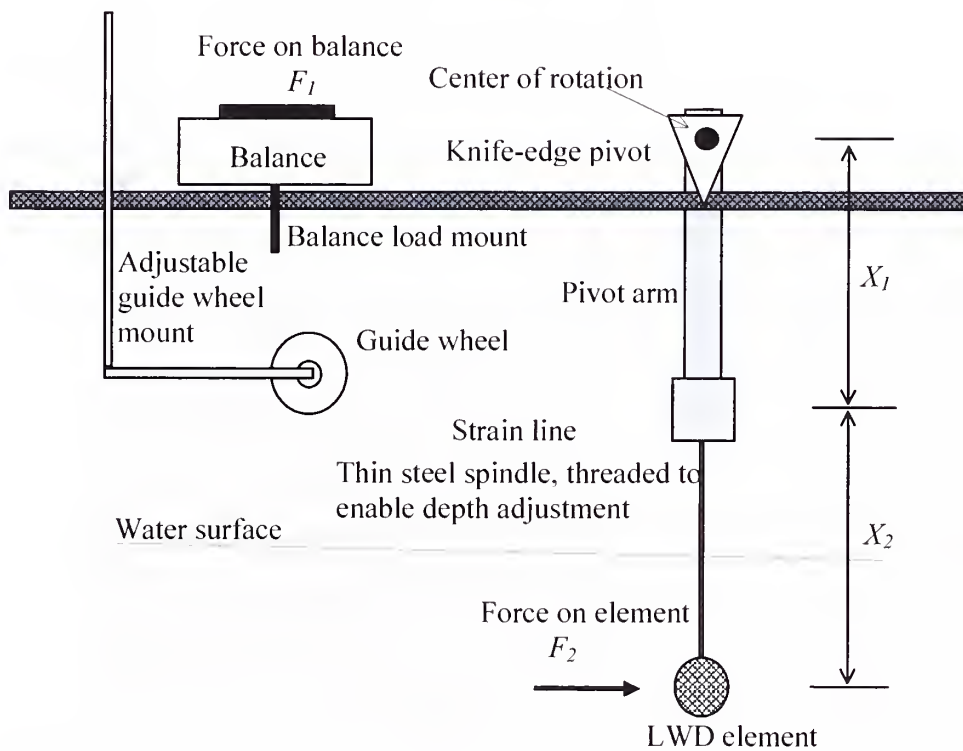
*Units are in centimeters*

**Figure 6: Schematic diagrams of LWD positions in the flume**





**Figure 7: Flume set-up**



**Figure 8: Strain gauge set-up**





**Plate 1: Model channel, showing scraper plate and pre-run channel geometry**



**Plate 2: Looking downstream along surface of channel, testing 0.1 m element**



Each LWD element had a thread drilled at the center of its long axis which enabled it to be screwed into a steel spindle which was in turn attached to a swinging arm that was suspended by knife edge pivots in a cradle attached to the flume top. Element height within the flow could be adjusted by sliding the spindle up and down within the pivoting arm between two locking nuts.

If the arm and spindle were free moving, force on the element would push it forward in the flow, the arm rotating about the pivot point. However, the pressure force was translated to a strain line made from fine fishing wire, which connected to a loading hook in the base of an electronic balance. Thus, force on the element was translated to a mass reading on the balance. An equivalent force reading was calculated using the equation:

$$F_1 = G_1 / \text{kg} \times g \quad (45)$$

where  $F_1$  = equivalent force reading on the balance (N),  $G_1$  = mass reading on the balance (grams),  $\text{kg}$  = conversion to kilograms (divide by 1000). Actual drag force on the element was determined by calculating the moment of force about the pivot point. Thus:

$$F_2 = (F_1 - F_0) X_1 / (X_1 + X_2) \quad (46)$$

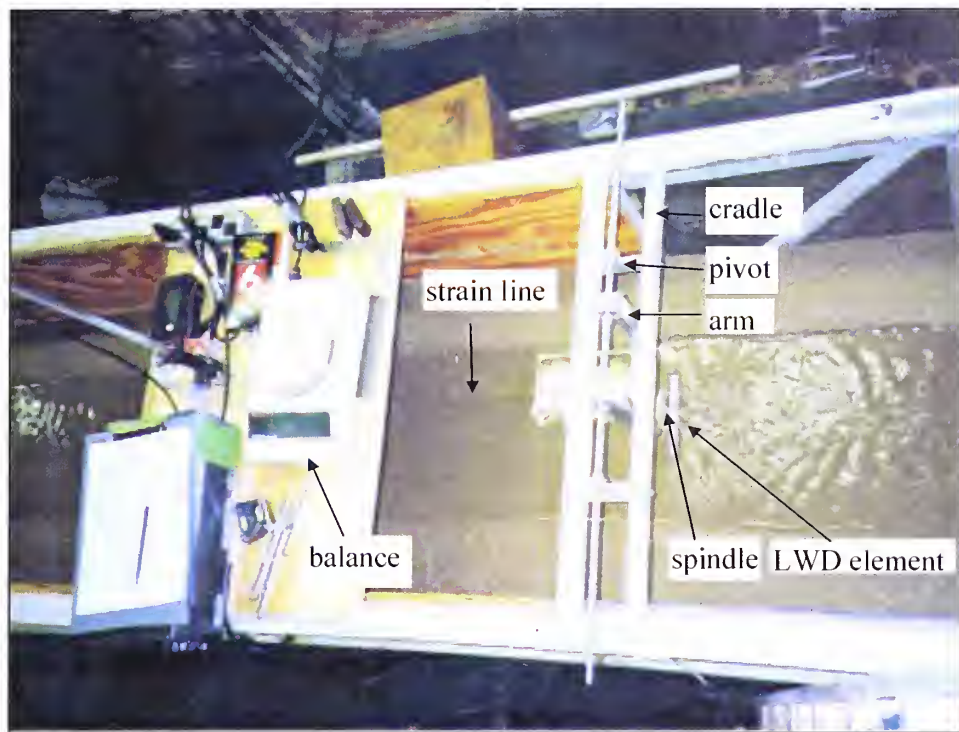
where  $F_2$  = drag force on LWD element (N),  $F_0$  = residual force reading on balance when there is no flow due to pre-loading tension in the strain line (N),  $X_1$  = distance from pivot point to strain line (m), and  $X_2$  = distance from strain line to center of element (m).

For each test run the channel was re-cut, smoothed and the design discharge run through for two hours prior to testing to ensure that the boundary remained stable. The element and strain gauge apparatus were then set up on the flume and the pivot arm lowered into its cradle, so that the LWD element became suspended in the flow at the appropriate depth and position relative to the channel cross-section. Plate 3 shows the strain gauge apparatus mounted on the flume during a test run.









**Plate 3: Experimental set-up, showing pivot arm and balance. Run with 0.1 m element**

Readings on the balance were then taken as soon as possible after element immersion and then at fixed time intervals which lengthened gradually as force readings declined asymptotically due to channel re-adjustment to an equilibrium form. Adjustment of the channel geomorphology was monitored during each run using a video suspended above the flume section and also noted by sight.

The largest element caused erosion and sediment transport that finally ceased after four hours of running time. Force readings therefore also decayed to a roughly constant value after this time period. The remaining elements were tested in order of size. Time until sediment transport ceased was found to decrease with element size but total monitoring time was maintained at four hours to ensure integrity in the resulting data-set. At the end of each test run the flume was drained and a detailed survey made of the channel topography in a section 1.2 meters long downstream from the element suspension position, using a point gauge mounted on the flume instrument carriage.



## 6 Description of the Flume Results

### 6.1 Introduction

There were two principle aims in the flume experiments: (1) to determine the scale, type and spatial extent of adjustment in channel geomorphology caused by Underflow, Dam, Deflector and Flow-Parallel debris elements in isolation from other channel adjustment processes such as degradation, and (2) to understand the hydraulic processes associated with simple LWD forms. Quantification of the hydraulic processes provides insight into the affect of LWD on flow field, velocity and shear stress within a channel reach, which in turn drive erosion and sediment transport processes thus linking LWD with specific geomorphic forms.

The forces acting on LWD elements can be determined by re-arranging the dimensionless drag coefficient equation (equation 2) to give:

$$F_D = 0.5 v^2 A_D \rho_w C_D \quad (47)$$

where  $F_D$  = Drag force (N).

There are three unknown quantities in the equation for a given LWD element ( $A_D$  is known). Force was measured directly in the experiments thus making it necessary to determine a drag coefficient for each element in order to solve the equation for approach flow velocity.

### 6.2 Expansion of flume results to prototype dimensions

The key to these flume experiments is that the model is scaled from a prototype river reach, maintaining dynamic, kinematic, and geometric similarity. It is therefore a legitimate procedure to re-scale the model results using the various scaling factors described earlier to produce force, velocity, time and geomorphic change dimensions for the prototype reach. By doing so, the hydraulic and geomorphic impact of LWD on sand bed rivers can be described.



The variables that required scaling to prototype dimensions from the model were: (1) time ( $T_m \rightarrow T_p$ ), (2) velocity ( $v_m \rightarrow v_p$ ), and (3) drag Force ( $F_m \rightarrow F_p$ ). Time data is scaled according to equation 28. Time scale ratio ( $T_r$ ) is therefore:

$$T_r = (59.667/27.142)^{0.5} = 1.48$$

Time in the prototype ( $T_p$ ) is thus derived from time in the model ( $T_m$ ) by:

$$T_p = T_m \times 1.48$$

Velocity data is scaled according to equation 27. The velocity ratio is therefore:

$$v_r = 27.142^{0.5} = 5.2$$

Velocity in the prototype ( $v_p$ ) is therefore derived from velocity in the model ( $v_m$ ) by:

$$v_p = v_m \times 5.2$$

Drag force is scaled according to equation 31. Water density in the model and prototype were assumed to be similar so that the water density ratio ( $\rho_r$ ) is equal to one. Drag force ratio ( $F_r$ ) is therefore:

$$F_r = 1 \times 59.667^2 \times 27.142 = 96629.6$$

Force in the prototype ( $F_p$ ) is therefore derived from force data in the model ( $F_m$ ) by:

$$F_p = F_m \times 96629.6$$

These scaling values were then used to convert model results to the prototype dimensions.

The flume model debris element dimensions also have to be re-scaled to prototype dimensions in order to make sense of the model data. Using the horizontal and vertical scaling relationships developed in section 4 dimensions for the prototype debris elements are listed in Table 7.

### **6.3 Limitations of the flume model**

There are three important differences between the flume model and the prototype that must be considered when interpreting the data. The prototype has a considerable sediment transport load through the channel at the  $Q_2$  discharge, whereas the flume model had no sediment transport, except for that caused by the LWD elements. In the field this transported sediment will obviously interact with LWD and may be deposited as bar formations in areas of the channel where the debris shields the flow, or causes



backwater effects. Such formations were observed in the field. As there was no sediment transport from upstream in the flume it is therefore likely that the volume and areal extent of bars created by each element would be less than those observed in the prototype.

<b>Representative Element Type</b>	<b>Element Length in Model (m)</b>	<b>Element Length in Prototype (m)</b>	<b>Element Diameter in Model (m)</b>	<b>Element Diameter in Prototype (m)</b>
Underflow	0.30	18.0	0.019	1.1
Dam	0.15	9.0	0.019	1.1
Deflector	0.10	6.0	0.019	1.1
Flow-parallel	0.07	4.2	0.019	1.1

**Table 7: Prototype debris element dimensions**

The composition of the banks of the prototype river is a mixture of materials with different structural properties. The banks of the base flow channel are often found to be non-cohesive sand, if the reach is stable or aggrading, or highly cohesive clay material if the channel is degrading. Bank angles in this region tend to be shallow ( $<40^\circ$ ). These materials are fluvially eroded through particle-by-particle entrainment. Above the base flow area, banks are often found to be composed of loess or a variety of different alluvial deposits. Bank angles in these materials tend to be close to vertical. These higher areas of the channel bank come into contact with the flow only during the less frequent events (remember if the creek has degraded, such events are unlikely to be ‘bankfull’), and tend to retreat mainly by mass failure as the lower bank material is fluvially eroded away. LWD tends to cause an increase in fluvial erosion on the bed and of the lower banks. This in turn results in mass failure of the upper bank, so that large block of material fall into the channel, onto and around, the debris accumulation. The flume, however, had banks composed solely of sand, with an consistent angle of 34 degrees. As accurate representation of more cohesive materials at that scale is virtually impossible. So, while the flume banks were of an angle and consistency roughly similar to that found in the low flow region of stable or aggrading channels, they were not representative of degrading channel environments, or bank material properties generally found higher in the bank





profile. LWD induced bank erosion in the flume therefore only occurred through direct fluvial action, as it was not possible to replicate the mass failure erosion mechanism. The resulting channel morphologies created in the flume will therefore only partially represent the forms that are found in the field, although we consider that bed features and lower bank erosion patterns will have been faithfully reproduced.

LWD jams in the field are complex. They have generally been found to form around a 'key' debris element such as a large tree. They also evolve over time becoming either larger and more impermeable as smaller debris transported from upstream piles up against the jam. The 'jams' in the flume, however, were very basic and represented 'key' debris element sizes and positions in the channel for the generalized Underflow, Dam, Deflector, and Flow Parallel jam classifications. It would have been virtually impossible to measure forces on a 'realistic' jam with a ramification of smaller and more complex element forms. Moreover, the consistency of element form (except for the all important length dimension) made it possible to attribute the difference in hydraulic and geomorphic results solely to the variation in area of flow blocked by the element.

It is virtually impossible to create a scale model of any natural channel environment without resorting to a considerable level of simplification. The simplification was necessary as the overall aim of these experiments was to understand the gross properties of river flow interaction with different sizes of tree like objects and the resulting potential effects had upon the channel boundary.



## 7 Discussion of Results

### 7.1 Drag coefficient calculations for simulated debris elements

Drag coefficient ( $C_D$ ) values for each of the four simulated debris elements were obtained by measuring the flow force on each element over a range of velocities in a separate, fixed boundary flume. The flume has a width of 1.22 m, and a length of 30.5 m. Approach flow velocities were measured using a pitot tube and velocity values averaged over a two minute sample period. Plate 4 shows the fixed boundary flume and force gauge apparatus. The force on each element was calculated by converting the average of five mass readings from the balance to a force (N) using equation 46.



**Plate 4: Force gauge set up in fixed boundary flume to calibrate drag coefficient values for each element.**

The residual value caused by the support spindle alone was subtracted from each reading and the actual force on the element calculated taking a moment about the spindle fulcrum. Drag force on each element was measured over a range of seven depths. Total flow depth during the test runs was 0.3 m. The results are presented in Table 8, which



also shows minimum and maximum balance readings at each depth, and element Reynolds and Froude numbers.

Figure 9 shows the relationship between drag coefficient and flow Reynolds number ( $Re$ ). The dark curve on the plot shows variation of  $C_D$  with  $Re$  for a smooth infinitely long cylinder in infinitely wide flow (White, 1979). For bodies with a finite length drag coefficient decreases as length is reduced because flow round the ends of a body reduces the pressure in front and increases the pressure behind it. Drag coefficient values for cylinders with a range of  $l/d$  ratios, published by White (1979), are shown in Figure 9 (top left hand box).

Drag results for the four elements are plotted on this graph as colored symbols. Ideally all the measured results should cluster about the  $l/d = \text{infinite}$  curve. There is some spread of the data however, both above, and below the curve. This spread can be explained in part because  $l/d$  ratios vary from 15 for the 0.3m element, down to 3.7 for the 0.07m element (see box in bottom left corner of the graph), so values can be expected to vary between elements, as suggested by White's (1979) data. White's data also indicates that objects of a finite length should have  $C_D$  values less than 1.2. However, and my experiments produced  $C_D$  values as high as 1.5 (refer to Figure 9, and notice that the plotted data extends above the  $l/d = \text{infinite}$  curve). We attribute this discrepancy to the fact that my experimental flume was quite narrow, so blockage effects (refer to section 2.2) will have been significant, whereas White's data assumes flow of infinite width (remember that blockage increases the drag coefficient).



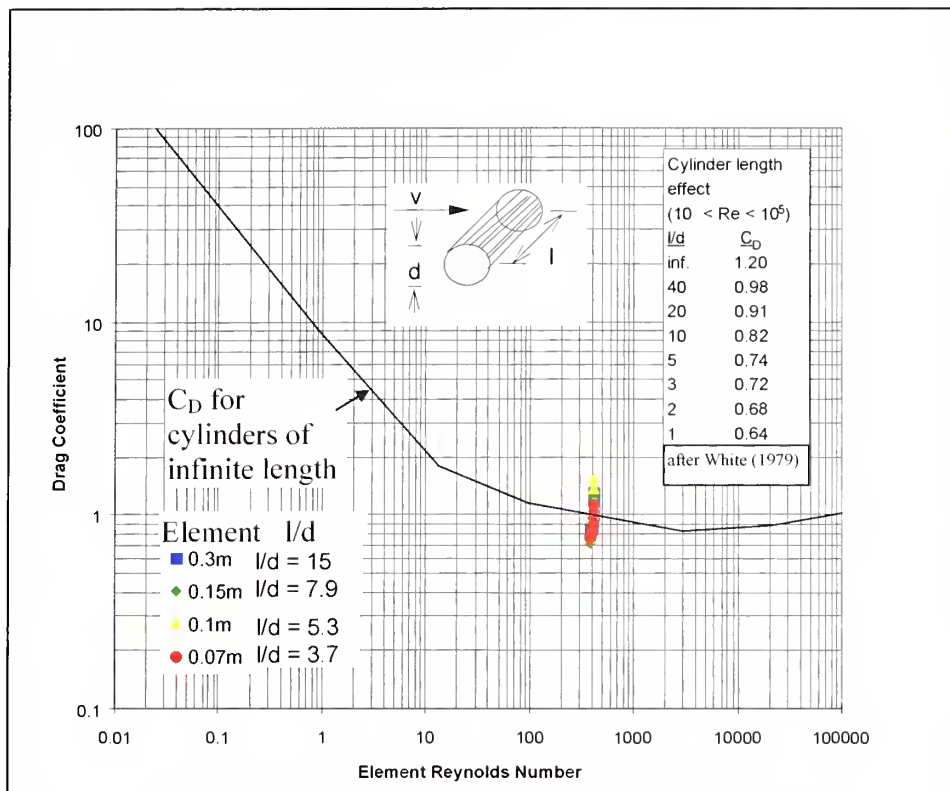
Element and velocity depth from bed (m)	Approach velocity (m/s)	Balance reading (g)	Min. reading (g)	Max. reading (g)	Residual reading (g)	Drag force (N)	Drag coefficient $C_D$	Reynolds number $Re_c$	Froude number $Fr_c$
<i>0.3 m element</i> [element area ( $A_D$ ) = 0.0057m <sup>2</sup> ]									
0.29	0.219	48.48	47.32	50.55	19.18	0.178322	<b>1.2801</b>	416.1	0.507
0.28	0.218	50.04	48.7	51.52	19.59	0.17633	1.3018	414.2	0.504
0.27	0.217	46.82	46.27	49.32	20.01	0.151177	1.1264	412.3	0.502
0.26	0.216	43.94	42.08	46.98	20.14	0.130772	0.9834	410.4	0.500
0.25	0.215	42.08	41.62	45.09	20.9	0.113474	0.8613	408.5	0.497
0.2	0.211	42.97	41.24	47.16	21	0.108009	0.8512	400.9	0.488
0.15	0.205	44.83	43.19	47.93	21.09	0.101802	0.8499	389.5	0.474
<i>0.15 m element</i> [element area ( $A_D$ ) = 0.00285m <sup>2</sup> ]									
0.29	0.219	27.11	26.32	27.72	12.7	0.085757	1.254	416.1	0.507
0.28	0.218	26.57	25.66	27.24	14.62	0.077988	1.151	414.2	0.504
0.27	0.217	27.37	26.98	28.01	14.48	0.072684	<b>1.083</b>	412.3	0.502
0.26	0.216	25.54	25.19	26.85	13.88	0.064067	0.9636	410.4	0.500
0.25	0.215	27.47	27.7	28.71	15.57	0.063755	0.9678	408.5	0.4979
0.2	0.211	27.95	26.21	27.3	14.23	0.054448	0.8582	400.9	0.4887
0.15	0.205	33.57	32.7	35.82	17.26	0.042239	0.7053	389.5	0.4748
<i>0.1m element</i> [element area ( $A_D$ ) = 0.0019m <sup>2</sup> ]									
0.29	0.219	21.07	20.09	21.78	13.93	0.069867	1.5334	416.1	0.507
0.28	0.218	22.34	21.3	22.59	14.37	0.061788	1.3686	414.2	0.504
0.27	0.217	23.2	22.6	23.79	15.39	0.050915	1.1382	412.3	0.502
0.26	0.216	22.2	21.95	22.95	14.21	0.043902	0.9904	410.4	0.500
0.25	0.215	24	23.51	24.19	15.33	0.04645	<b>1.0577</b>	408.5	0.497
0.2	0.211	25.84	24.88	26	16.35	0.040681	0.9618	400.9	0.488
0.15	0.205	25.98	24.87	26.02	16.62	0.030403	0.7613	389.5	0.474
<i>0.07m element</i> [element area ( $A_D$ ) = 0.0013m <sup>2</sup> ]									
0.29	0.219	18.83	19.12	19.98	12.9	0.035291	1.1320	416.1	0.507
0.28	0.218	19.81	23.86	20.38	14.33	0.031734	1.0272	414.2	0.504
0.27	0.217	18.5	19.3	19.36	13.26	0.029547	0.9653	412.3	0.502
0.26	0.216	18.02	18.67	22.7	13.07	0.027198	0.8968	410.4	0.500
0.25	0.215	21.7	22.08	23.34	16.96	0.025395	<b>0.8451</b>	408.5	0.497
0.2	0.211	22.72	24.85	23.25	17	0.023342	0.8065	400.9	0.488
0.15	0.205	21.35	21.9	22.02	16.46	0.020969	0.7677	389.5	0.474

where force (N) = mass (g) / 1000 kg x 9.81, drag coefficient = force / ( $\rho \times 0.5 \times A_D \times v^2$ ), element Reynolds number  $Re_c = v d / \nu$ ,  $d$  = element diameter (0.019 m), and element Froude number  $Fr_c = v / \sqrt{g d}$ .

**Table 8: Drag coefficient on elements at a range of depths in infinite flow**







**Figure 9: Element drag coefficient as a function of Reynolds number**

It is evident from Table 8 that drag coefficients for each element tend to increase with distance from the bed. This is due to the increase in flow velocity towards the flow surface. This relationship becomes more evident if the drag coefficient results are plotted as a function of relative flow depth (Figure 10). Relative flow depth is defined as total flow depth ( $d$ ) divided by the depth from the center of the element to the channel bed ( $Y$ ). Drag coefficient increases slowly with relative depth below  $Y/d$  of 0.85. However, above this level drag coefficient increases rapidly to a maximum at the flow surface. This accelerated increase in drag close to the water surface can be attributed to a phenomenon known as wave drag. This occurs when a submerged obstruction in flow begins to disturb the flow surface, setting up surface waves. Energy is required to create these surface waves which consequently means that more drag is being imposed by the object on the flow than the simple disturbance of stream lines around the object. These data show that drag coefficients may be significantly underestimated if generally estimated



coefficients are used to characterize bluff bodies without considering the objects proximity to the fluid free surface.

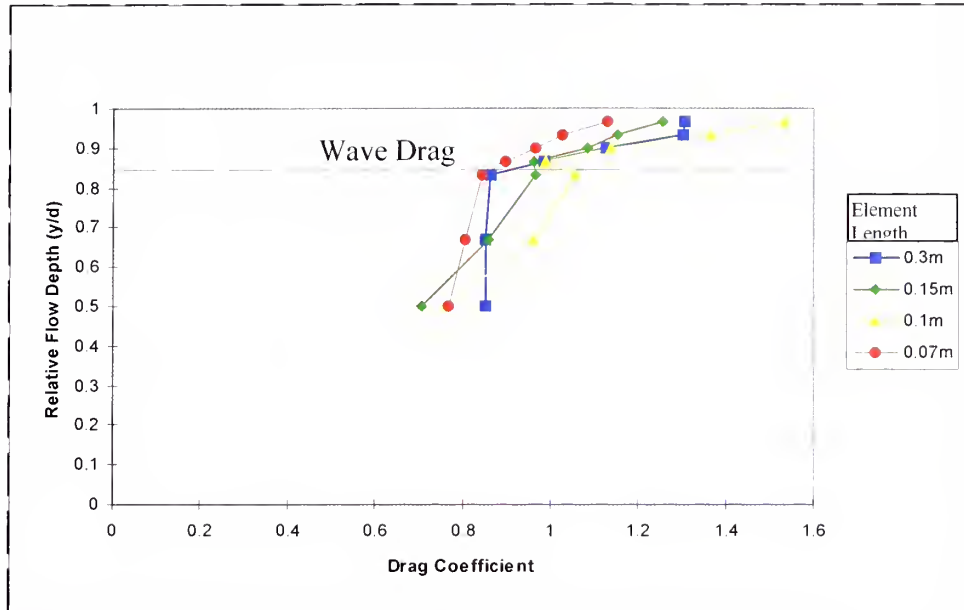


Figure 10: Drag coefficient as a function of relative flow depth

## 7.2 Selection of drag coefficient values

The drag coefficient values for each LWD element determined in the fixed boundary flume were then used to solve equation 47 to determine approach flow velocities in the Abiaca Creek model. Values selected were those corresponding to the appropriate element depths in the model and these values are highlighted in bold in Table 8 and displayed in Table 9.

Element length (m)	Depth of flow from surface to element center (cm)	Corresponding drag coefficient value from Table 8
0.07	4.0	0.84
0.10	4.0	1.05
0.15	2.5	1.08
0.30	0.5	1.28

Table 9: Drag coefficient values used to solve equation 47



### 7.3 Estimation of friction factor due to LWD

Shields and Gippel (1995) developed a method for estimating Darcy-Weisbach friction factor due to LWD based upon the work of Smith and Shields (1992). They express total friction factor as:

$$f_{\text{total}} = f_{\text{grain}} + f_{\text{bedform \& bar}} + f_{\text{bends}} + f_{\text{debris}} \quad (48)$$

Friction factor due to grain resistance ( $f_{\text{grain}}$ ) is defined by equation 7 while friction factor due to bends ( $f_{\text{bends}}$ ) and bedforms and bars ( $f_{\text{bedform \& bar}}$ ) must be estimated. The proportion of channel roughness ascribed to debris is determined to be:

$$f_{\text{debris}} = \frac{4}{\alpha} \times \frac{\sum_{i=1}^n C_{Di} A_{Di}}{wL} \quad (49)$$

where,  $\alpha$  = kinematic energy correction factor (roughly 1.15), and  $i$  = debris element 1, 2, etc.

Equation 49 is used to estimate friction factor created by the LWD elements in the model flume. These values can be compared with measurements reported by Shields and Gippel (1995) from data taken from the Obion River (Tennessee) and the Tumut River (Australia), and with estimates of friction factor for the prototype reach on Abiaca Creek reported by Watson et al. (1993).

Drag coefficients used to solve equation 47 were those presented in Table 9. Results are shown in Table 10. Comparison of these results with those presented by Shields and Gippel (1995) (see Table 11) demonstrates that values calculated for the flume model are of the same order of magnitude as those estimated in the field situation.

The flume model can therefore be regarded to have accurately re-created the average drag and friction factor properties of LWD as found in the field.

Total friction factor in the prototype reach on Abiaca Creek is suggested by Watson et al. (1993) to be  $n = 0.032$ . Converting this value to a Darcy-Weisbach friction factor using the following equation (Richards, 1982):



$$f = 8gn^2 / R^{1/3} = 0.235$$

(50)

Element Length (m)	C <sub>D</sub> in infinite flow	Element area normal to flow (m <sup>2</sup> )	f <sub>debris</sub>	f <sub>g</sub>	F <sub>total</sub>
0.30	1.28	0.0057	0.051	0.146	0.200
0.15	1.08	0.0029	0.022	0.146	0.168
0.10	1.05	0.0019	0.014	0.146	0.160
0.07	0.84	0.0013	0.008	0.146	0.154

**Table 10: Calculation of Darcy-Weisbach friction factor due to LWD**

Site	Q (m <sup>3</sup> /s)	V (m/s)	S (m/km)	R (m)	D <sub>50</sub> (mm)	f <sub>bed</sub>	f <sub>bends</sub>	f <sub>debris</sub>	f <sub>total</sub>
Obion River	3.9	0.29	0.63	0.9	0.27	0.22	0.00	0.20	0.42
Obion River	4.0	0.33	0.61	0.7	0.44	0.16	0.00	0.18	0.34
Obion River	9.0	0.46	0.78	1.1	0.44	0.17	0.00	0.17	0.34
Obion River	16.2	0.53	0.45	1.6	0.27	0.11	0.00	0.04	0.16
Obion River	16.9	0.65	0.51	1.4	0.44	0.09	0.00	0.02	0.11
Obion River	36.9	0.72	0.46	2.7	0.27	0.11	0.00	0.07	0.18
Obion River	40.5	0.86	0.60	2.5	0.44	0.10	0.00	0.03	0.13
Obion River	40.9	0.77	0.49	2.7	0.27	0.10	0.00	0.07	0.17
Obion River	41.3	0.86	0.59	2.5	0.44	0.10	0.00	0.03	0.13
Obion River	3.6	0.46	0.42	0.5	0.44	0.06	0.00	0.03	0.11
Obion River	4.2	0.45	0.54	0.6	0.57	0.09	0.00	0.00	0.09
Obion River	10.7	0.57	0.42	1.2	0.57	0.08	0.00	0.06	0.14
Obion River	22.2	0.84	0.46	1.6	0.57	0.06	0.00	0.01	0.07
Obion River	47.9	0.91	0.52	2.7	0.57	0.09	0.00	0.01	0.10
Obion River	53.2	0.98	0.54	2.8	0.57	0.08	0.00	0.01	0.10
Tumut River	112	1.01	1.10	2.8	16.0	0.11	0.04	0.02	0.17
Tumut River	96	0.90	1.00	2.9	22.0	0.13	0.07	0.03	0.22
Tumut River	96	0.90	1.50	2.9	28.0	0.14	0.12	0.00	0.26
Tumut River	125	1.08	1.30	3.0	16.0	0.10	0.04	0.00	0.14
Tumut River	92	0.93	0.90	2.6	22.0	0.13	0.06	0.00	0.19
Tumut River	92	0.93	1.50	2.6	28.0	0.14	0.11	0.00	0.25

**Table 11: Computation of Darcy-Weisbach friction factor in the Obion River and Tumut River (after Shields and Gippel, 1995)**

This prototype value lies outside the upper range of  $f_{total}$  values predicted in Table 10. Considering that the prototype reach contains bed features that are incorporated into friction factor in equation 50 but were not present in the model situation, it would appear that Watson's field estimate of total friction factor is somewhat low. This may be due to neglecting the important influence of LWD.

From the model flume results, and those presented by Shields and Gippel (1995) it may be concluded that friction factor in natural channels may well be considerably underestimated. This is because even if resistance caused by bends and bedforms is





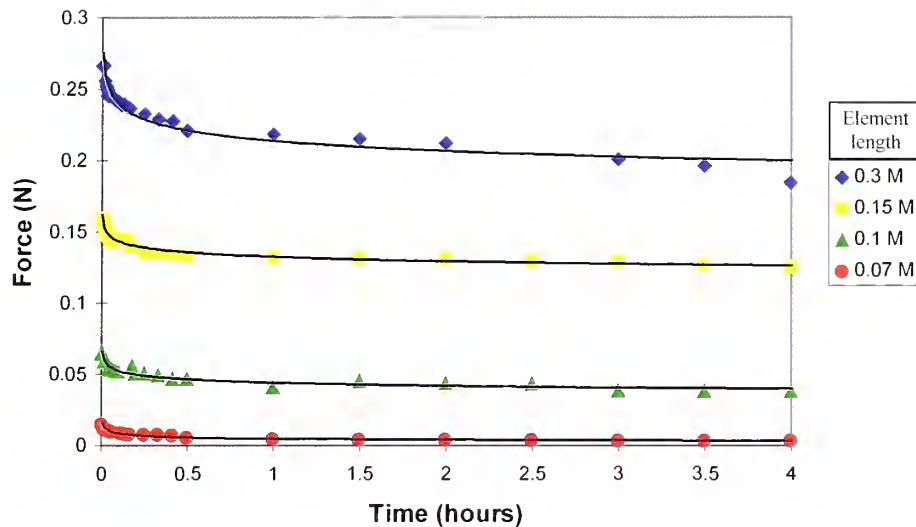
taken into account, reach averaged resistance due to debris accumulations is rarely considered but can create as much frictional resistance, if not greater than the resistance offered by channel bed roughness (see Table 11).

#### **7.4 Drag force on LWD elements in the model**

Drag force on each element is plotted against time in Figure 11. The temporal change in force readings can be explained by the fact that as an element was lowered into the model channel, flow was forced to accelerate past it in order to maintain continuity of discharge. The affect of flow acceleration and increased turbulence was to raise boundary shear stress above the threshold condition causing the channel bed and banks to scour in the vicinity of the element. The scoured sediment was carried downstream and deposited where flow decelerated to the point of losing competence to maintain transport. However, the rate of scouring declined over time because as the cross-sectional area of the channel increased so velocities fell again thus reducing boundary shear stress. This negative feedback between channel enlargement and boundary shear stress reduction eventually led to an equilibrium state once more, where the channel boundary returned to a threshold state, but with a new, enlarged cross-sectional area. Flow velocity around the element therefore decayed in an asymptotic manner through time, causing the drag force experienced by the element to decline in a similar manner.

Power functions are often found to best characterize changes in energy and landscape adjustment in geomorphic systems (Thorn, 1988). This fact gave the justification for fitting power functions to the model data, and regression analysis demonstrates that power decay functions describe the measured changes in drag force very well. The equations of these functions and their respective  $r^2$  values are shown in Figure 11 and in Table 12.





**Figure 11: Measured change in drag force over time on each LWD element in the flume model**

Element Length (m)	Equation constant (a)	Equation Exponent (b)	Goodness of fit (r <sup>2</sup> )
0.30	0.213	-0.048	0.94
0.15	0.132	-0.034	0.95
0.10	0.044	-0.075	0.92
0.07	0.004	-0.249	0.97

**Table 12: Equations describing drag force decay on LWD elements. Regression Functions take the form:  $\text{Force} = a + \text{Time}^b$**

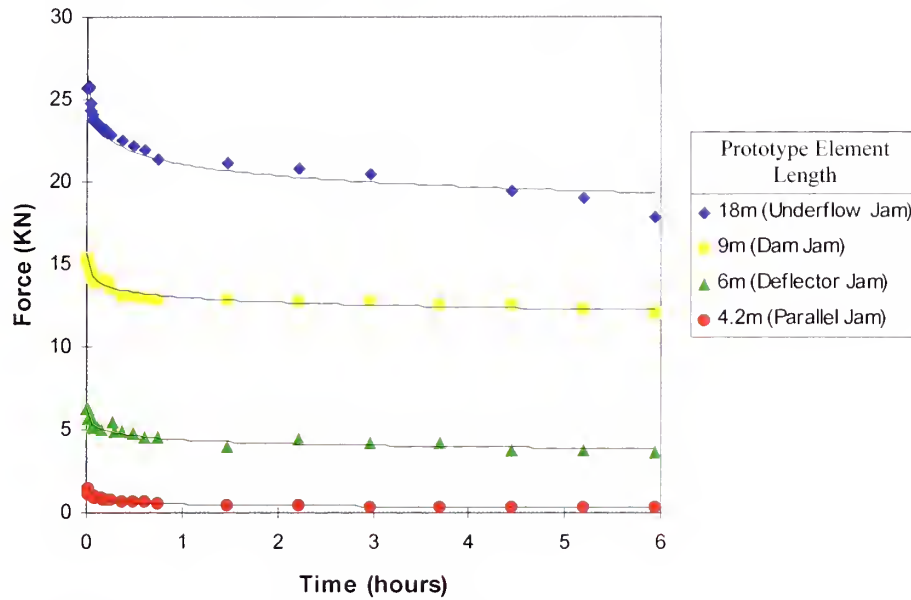
It is evident from Figure 11 and Table 12 that the larger the element the greater the total force acting upon it.

### 7.5 Drag force on LWD elements in the prototype

Figure 12 shows the change in drag force over time on LWD elements in the prototype reach (Abiaca Creek) computed from the model data. The distribution of the data is obviously the same as for the model, but absolute values have been expanded according to the force and time scaling relationships described in section 7. Note that drag force is measured in kilonewtons and that the time scale extends up to 6 hours. Prototype debris element dimensions shown in Figure 12 are calculated in Table 7.



Power functions have been fitted to the data and both the equations and  $r^2$  values are shown in Table 13. The shape of each fitted functions is obviously the same as for the model data, the actual values are simply larger in accordance with the scaling ratios.



**Figure 12: Change in drag force over time on LWD elements in the prototype reach computed from model data**

Element Length (m)/ Jam type	Equation constant (a)	Equation Exponent (b)	Goodness of fit ( $r^2$ )
18m	21.059	-0.048	0.94
9m	12.987	-0.034	0.95
6m	4.400	-0.075	0.93
4.2m	0.515	-0.241	0.98

**Table 13: Equations describing drag force decay on LWD elements in the prototype. Regression Functions take the form:  $\text{Force} = a + \text{Time}^b$**

For example, we can expect in the prototype river during a  $Q_2$  discharge event that a tree trunk with a length of 18 m and a diameter of 1.1 m will experience a drag force of 25.5 kN when it falls into the channel, normal to the flow, and that this drag force will decrease over a period of 6 hours to 17.5 kN. If one assumes that total force decay time



is equivalent to the time it takes the channel morphology to adjust, the geomorphic changes to a sand-bed creek caused by LWD elements are complete after a short period of time. Obviously, if a tree were to fall into such a creek while flow conditions were less than the 2-year event total force, adjustment times would be longer by an amount proportional to the approach flow velocity for that discharge.

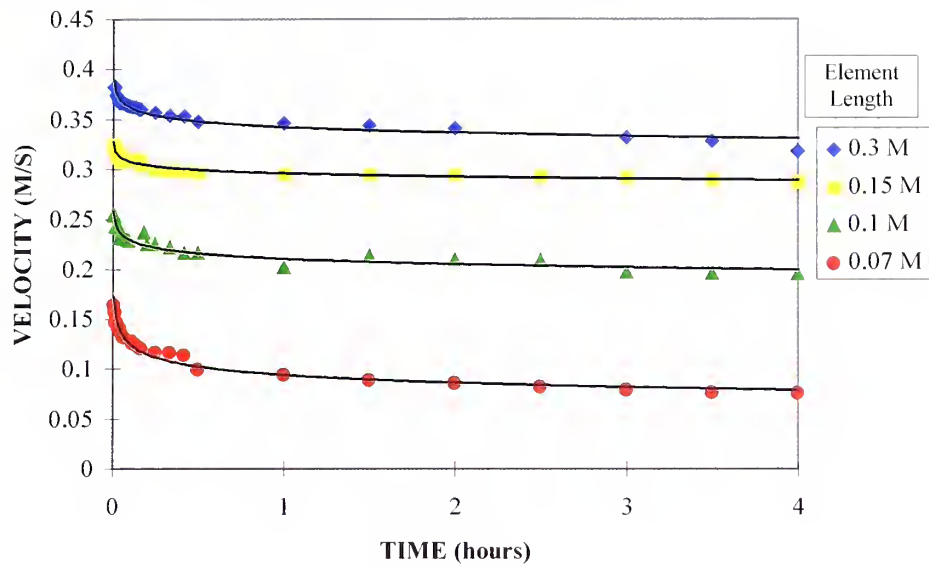
It can be concluded that the range and temporal change in values in Abiaca Creek caused by the channel boundary adjustment would be very similar to those predicted by the flume model. Given that the prototype reach was chosen as representative, these results must also be more generally applicable to LWD interaction with the flow in any sand-bed river in Northern Mississippi.

#### **7.6 Incident flow velocity on LWD elements in the model**

Change in incident velocity on each element over time was computed by substituting the measured drag force data (Figure 11) and drag coefficient values (Table 8) into equation 47. The results are displayed in Figure 13. Given that all other variables in equation 47 are constant for each time step except drag force, it is not surprising to find that incident flow velocity on each element decays over time in exactly that same manner as for the drag force measurements. The data were fitted by power decay functions, and function constants, exponents, and goodness of fit ( $r^2$  values) for each element are displayed in Table 14.







**Figure 13: Change in approach velocity over time on LWD elements in the flume model**

Regression Functions take the form: Velocity = a + Time <sup>b</sup>			
Element Length (m)	Equation constant (a)	Equation Exponent (b)	Goodness of fit (r <sup>2</sup> )
0.3	0.342	-0.024	0.94
0.15	0.296	-0.017	0.95
0.1	0.210	-0.037	0.92
0.07	0.094	-0.124	0.97

**Table 14: Equations describing incident velocity decay at each LWD element in the model**

It might be expected that these velocity curves would converge towards an asymptotic value over time as an equilibrium state is reached in the channel through the course of channel adjustment. It is also surprising that two curves in Figure 13 fall below the mean flume flow velocity of 0.24 m/s because velocities near the elements must have been considerably higher in order to cause sediment transport. These anomalies can be explained by the fact that elements were not suspended at the same depth in the model. The 0.3 m element was held just below the flow surface while the 0.15 m, 0.1 m and 0.07

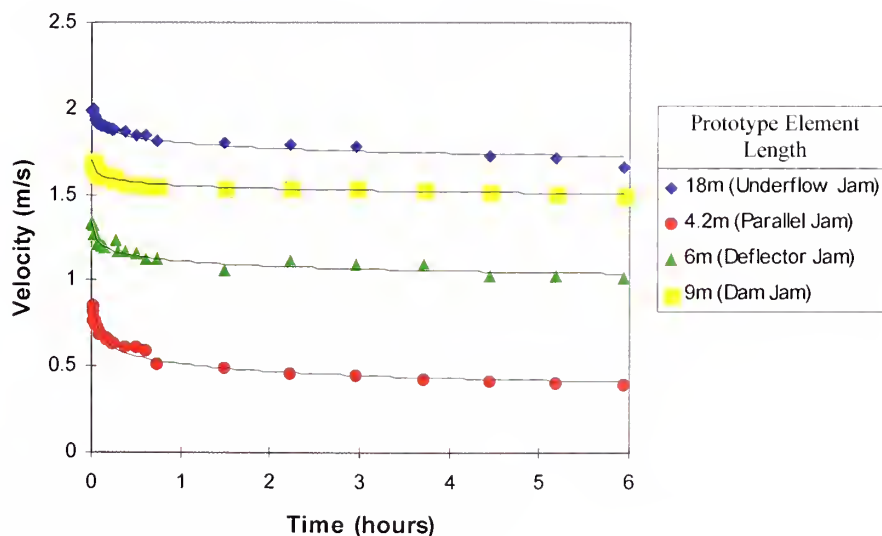


m elements were suspended at progressively greater depths in the flow. Larger elements will have experienced higher approach flow velocities than smaller elements, regardless of the disturbance caused by the element itself.

Figure 13 clearly demonstrates that the increase in flow velocity caused by the elements reduction of the channel cross sectional area is quickly accommodated by the channel. This occurred through erosion of the channel boundary causing velocity to fall in an asymptotic manner over time until boundary shear stress returned to the critical value and sediment transport ceased.

### 7.7 Incident flow velocity on LWD elements computed for the prototype

Figure 14 shows the change in approach flow velocity for the four different jam types as predicted for the prototype. Power decay functions have also been fitted to these data. The fitted equation constants, exponents and goodness of fit  $r^2$  values are shown in Table 15.



**Figure 14: Change in LWD element approach flow velocity over time in prototype reach computed from model data**



Element Length (m) / Jam Type	Equation Constant (a)	Equation Exponent (b)	Goodness of Function Fit ( $r^2$ )
18m	1.801	-0.024	0.94
9m	1.553	-0.017	0.95
6m	1.113	-0.038	0.93
4.2m	0.515	-0.125	0.98

**Table 15: Equations describing incident velocity decay on LWD elements in the prototype. Regression Functions take the form:  $\text{Velocity} = a + \text{Time}^b$**

The behavior of velocity change for each jam type is the same as that discussed for the model data but actual values are larger. Thus, maximum total adjustment time in the prototype is 6 hours. One can expect during a  $Q_2$  discharge event that a tree trunk with a length of 18 m and a diameter of 1.1 m will experience an incident flow velocity of 0.385 m/s when it falls into the channel, normal to the flow, and that this velocity will decrease over a period of 6 hours to 0.338 m/s.

### 7.8 Conclusions from the hydraulic data

The prototype drag force and incident velocity results lead to the conclusion that LWD obstructions are quickly accommodated for by geomorphic adjustment in mobile sand-bed channels. So, even dense LWD jams in sand-bed rivers will not disturb the reach-scale flow regime to the extent that general scour (i.e. bed degradation) might be triggered. Only local bed and bank adjustments are likely. It can be further concluded that LWD in sand-bed channels that are undergoing degradation and lateral adjustment as described by the Schumm et al. (1984) Channel Evolution Model is unlikely to act as a significant structural barrier to stop or slow the upstream migration of a knick-point. In short, the flow will very quickly erode both the bed and banks in the immediate vicinity of a jam to bypass the obstruction. LWD in sand-bed rivers is unlikely to alter the gross long-term energy balance (the ratio of potential to kinetic energy) of a reach by significantly damming up the flow, a finding which is a direct contrast to that reported by Marston (1982) for LWD jams in gravel bed rivers.

The geomorphic features associated with LWD jams in unstable sand-bed rivers are assumed to become relatively stable very quickly after the debris has entered the channel.



These conclusions agree with field observations as the local channel geomorphology, such as upstream and downstream bars and the depth and extent of scour holes, at the majority LWD jams monitored over the two year survey period varied very little over time. Indeed, local bank failure scars and in-channel bars caused by the six new jams that had formed in the survey reaches between the 1995 and 1996 were found to have already been colonized by a dense vegetation of grasses and shrubs by the time of the second survey.

### **7.9 Geomorphic results: Flume**

The previous discussion has focused on the hydraulic effects of the LWD elements. The next step is to examine how these effects interact with the channel boundary to produce a set of LWD induced geomorphic features.

At the end of each test run, once all sediment transport had been observed to cease, the discharge in the flume was gradually reduced until all flow drained into the sand underneath the cut channel. The flume was then surveyed along a length from 0.1 m upstream of the LWD element position to a point where channel topography was no longer disturbed downstream of the elements. A point gauge, mounted on the instrument carriage, was used to measure break of slope across the channel at regular distances down the flume, which thus produced a set of x,y,z data describing the channel topography. This data was then entered into a surface interpolation program that generated contour maps of the channel. The channel was also surveyed prior to each test run and a surface generated. These data enabled the generation of contour maps of relative channel adjustment by subtracting the pre-test surface from the post-test surface. The resulting contour surfaces for each test are shown in Figures 15 and 16. The uneroded channel 'floodplain' between the channel bank top and the flume sidewalls is colored in gray (marked left and right banks), without a contour surface in order to avoid confusion over the channel limits.

In Figures 15 and 16, there are the two bands of aggradation running in parallel strips along the channel at about 0.2 and 0.45 m across the channel. These bands with heights





of roughly +40 mm represent upper-bank material that has been dislodged by surface flow disturbances slumped to the bank base. The upper bank regions show this sediment removal and slumping.

A second set of features of great significance are the waves of upper bank scour, seen on the floodplain edge that become more pronounced the larger the element. These waves of scour are not related to the zones of bed and bank scour caused by flow impingement on the channel bed and lower bank. Instead they are caused by flow surface waves hitting the channel banks. These waves are generated by the combined effect of surface gravity waves set up by flow acceleration under the elements and by the closure of pressure generated streamlines around the element ends (White, 1994). The form and effect of the waves are shown schematically in Figure 17. The closer an object is to the flow surface, the more pronounced the water waves. This explains why the 0.15 m and 0.3 m elements (which lay at 0.20 and 0.05 m below the free surface) have created more pronounced nodes of scour than the 0.07 m and 0.1 m elements (which both lay at 0.35 m below the free surface). Plate 5 shows the topographic results of the 0.15 m element. The first set of pressure-generated waves on the downstream side of the element are clearly visible, as is the zone of element induced flow disturbance, that diminishes with distance downstream. This contrasts with the calm flow conditions approaching the element (left-hand side of the picture). The largest volumes of bank erosion were caused by deflection of subsurface flow due to flow acceleration around the LWD elements.



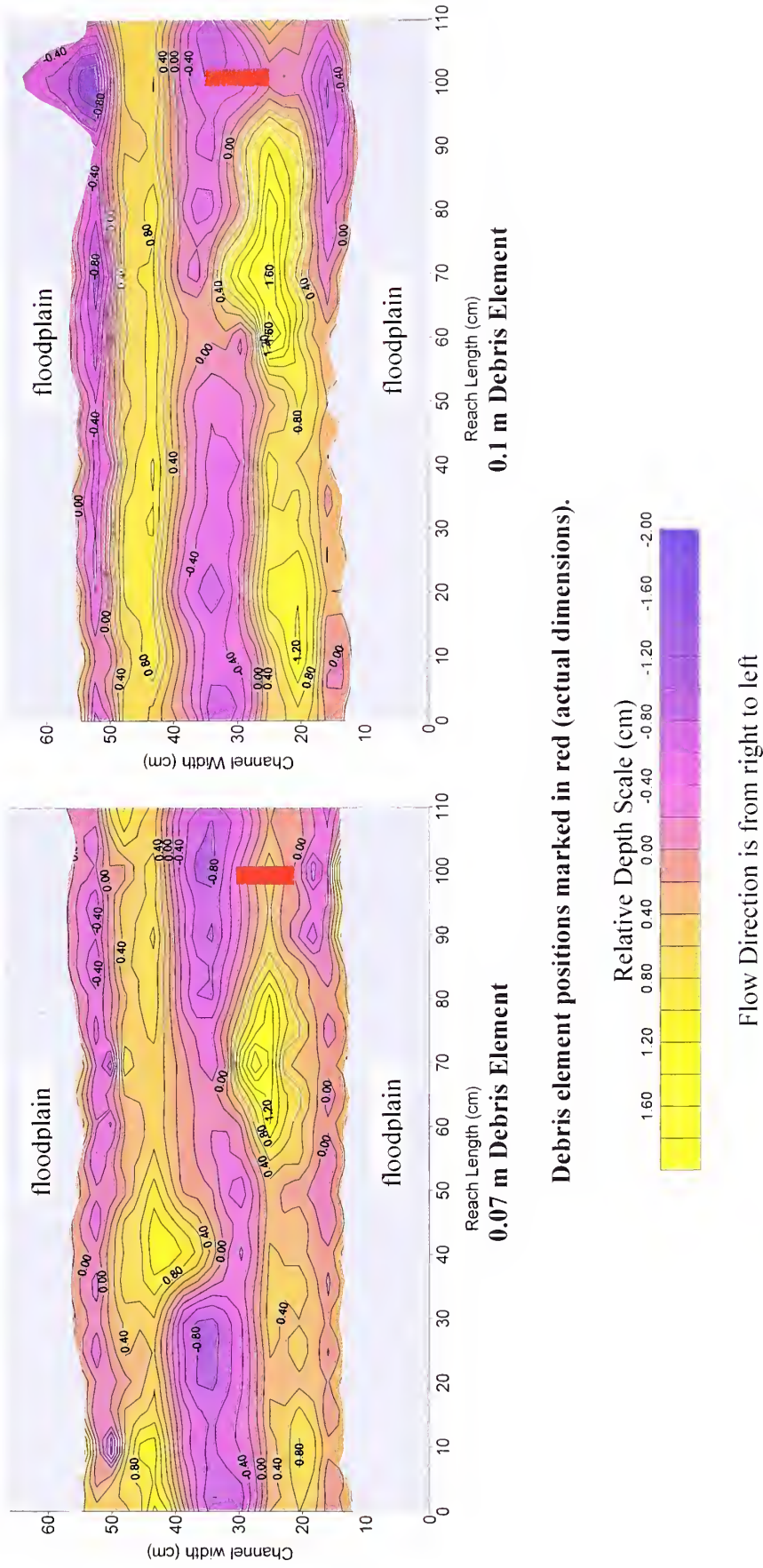


Figure 15: Contour plots of relative depth change for the flume model: 0.07 m and 0.1 m debris elements



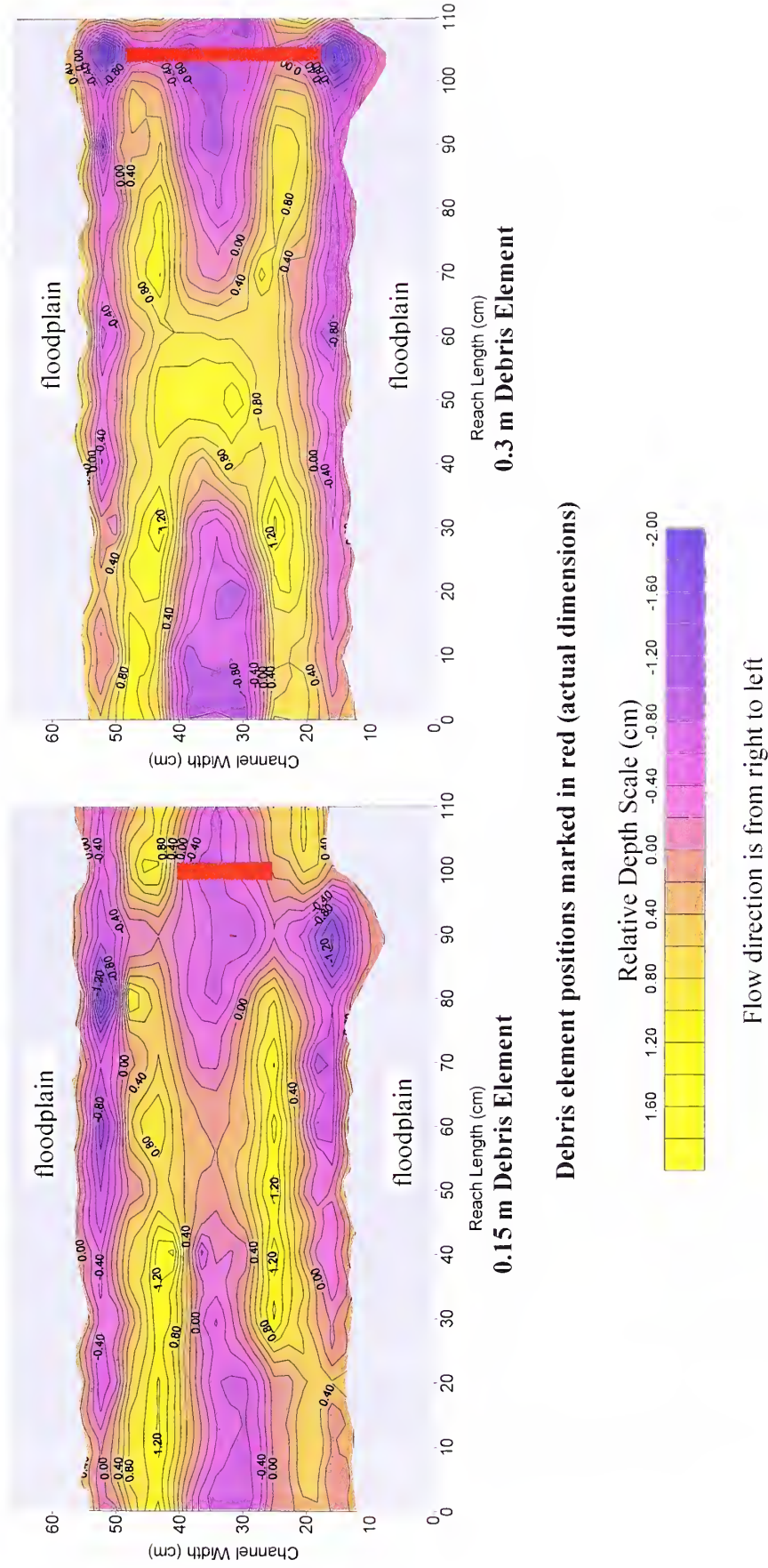


Figure 16: Contour plots of relative depth change for the flume model: 0.15 m and 0.3 m debris elements





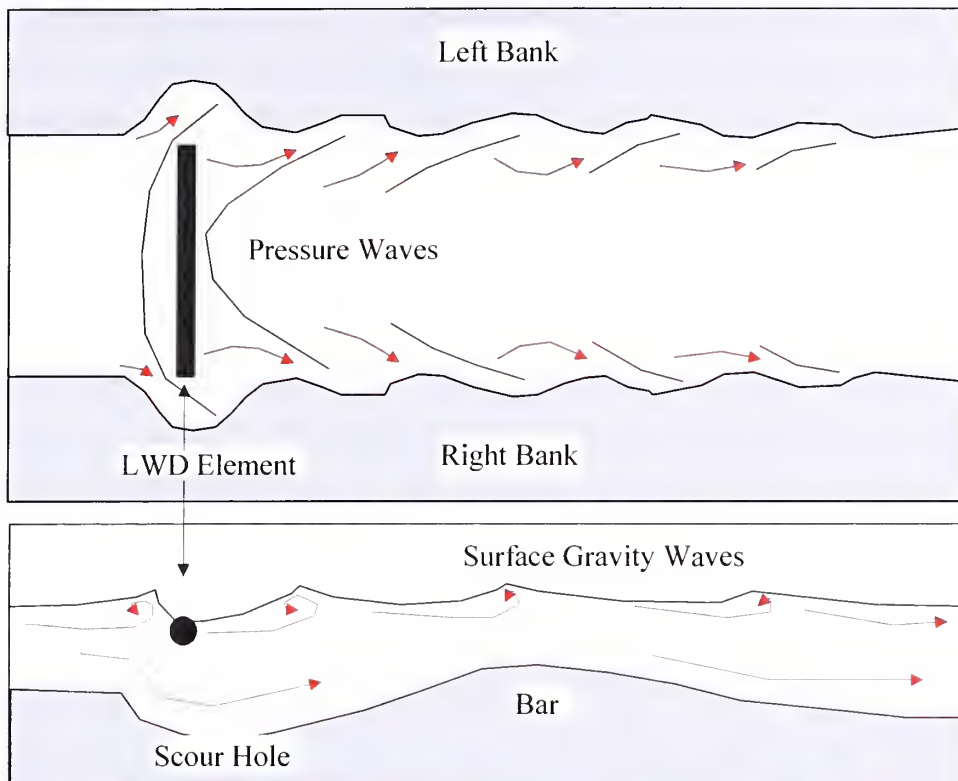


Figure 17: Geomorphologic impact of surface waves generated by LWD elements.



Plate 5: Flow disturbance created by the 0.15 m debris element





It is worth noting that the bank tops were located at 0.15 m and 0.53 m across the channel from the left flume side-wall prior to element immersion. All four elements can therefore be seen to have caused floodplain failure along the length of the survey reach.

The 0.1 m (deflector) debris element created the greatest local bank erosion (almost 0.1 m into the right floodplain) because it diverted a large part of the central fast flowing water from left to right across the channel. The resulting bank failure contrasts greatly with the limited bank erosion generated by the 0.07 m (flow parallel) element, which is only 0.03 m shorter, but lay closer to the base of the left bank and therefore did not disturb the central fast flowing stream. The 0.15 m (Dam) element split the flow into two streams that impinged on each bank downstream of the element. This caused scour of the left bank to a maximum depth of 12 mm net erosion, and a more elongated but narrower band of erosion along the right bank to a maximum depth of 15 mm net erosion. The eroded material was transported downstream across the bank face and deposited, as lateral bars in the zone of low shear stress that occurs at the break of slope between the bank and bed. The 0.3 m element lay close to the flow surface, spanning the full width of the channel. This meant that flow was deflected underneath the element but also around either end which produced two zones of high shear stress, eroding the banks up to a depth of 0.02 m of net change.

The location and severity of erosion depends on the size of the debris element but more importantly upon its position, both vertically in the flow stream and laterally across the channel, relative to the core of maximum flow velocity (White, 1994). The degree of flow impingement on either bank was greatest for the 0.15 m and 0.1 m elements for this very reason. In contrast the 0.07 m element created little bank failure as it did not interfere with the main flow stream. While the 0.3 m element caused the greatest net bank erosion in small zones at either end of the element, erosion downstream was limited. This is flow was diverted mainly under the obstruction parallel to the banks, rather than laterally across the channel that set up a back and forth oscillation of the flow field in the downstream reach.



The second component of geomorphic change was adjustment of the channel bed topography by the disturbed flow field (refer to Figures 15 and 16). The 0.07 m element created a scour hole in the center of the channel that was 8 mm deep at its maximum. The sand scoured from this hole was deposited mainly in the zone of calm water in the wake of the element, forming a lateral bar 14 mm high and 0.3 m long against the left bank. A second bar formed at the base of the opposite bank, slightly further downstream, where the flow turbulence diminished. Flow then oscillated very slightly between these two features. This pattern of sedimentation resembles a set of 'alternate bars' (Richards, 1982) that are common features in straight sections of both sand and gravel bed rivers. A second zone of bed scour developed downstream of the alternate bars. This secondary scour feature was observed to occur downstream of the zone of sediment deposition and is thought to have been caused by flow acceleration over the crest of and between the bar formations.

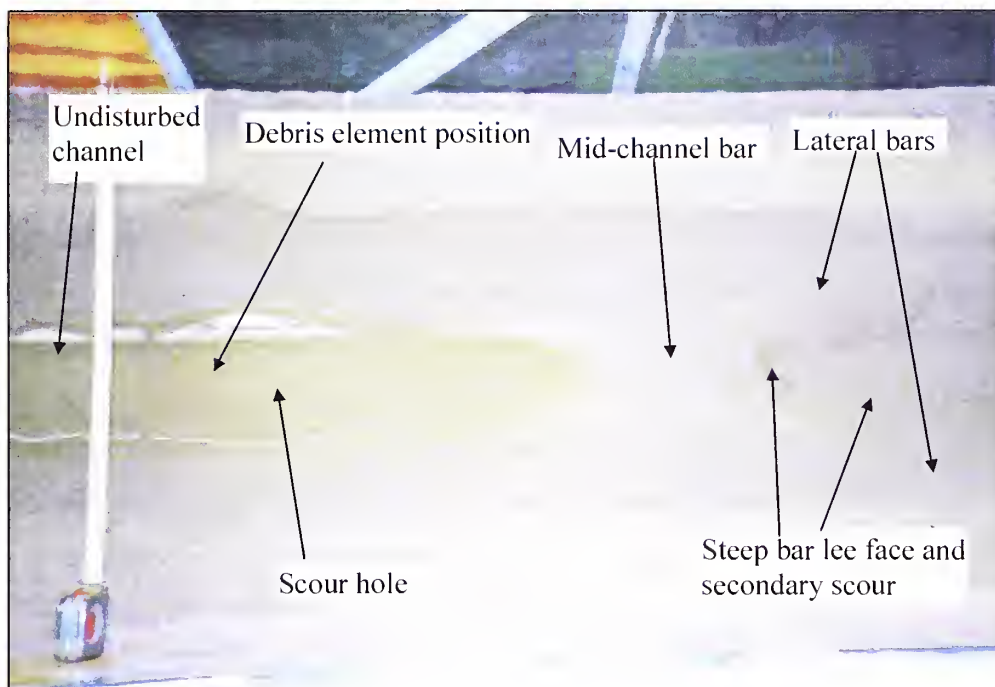
The 0.1 m element produced a large bar in its wake, which was 0.35 m long and 13 mm high. The material that built this bar came mainly from the area of intense bank erosion, slightly upstream on the opposite bank, and was carried across the channel by high-energy, sediment-laden flow to the area of low energy in the element's lee. A second, elongated but lower bar formed against the base of the right bank running between 0.05 m and 0.75 m along the survey reach. A third shorter bar formed against the base of the left bank at the very downstream end of the survey reach. This pattern of alternating bars demonstrates that the element set up an oscillatory flow pattern in the downstream reach. The erosive strength of this meandering flow was, however, dissipated after the initial deflection to the right bank. It is therefore evident that such an obstruction could not disturb the flow field to the extent that reach scale channel meandering might be induced. Bed scour also occurred underneath the element but the extent and depth of this feature was not as great as that created by the 0.07 m element.

The 0.15 m element's position in the center of the channel caused a large body of the flow to be diverted downwards onto the channel bed producing a large scour hole 0.4 m long and up to 8 mm deep. The sediment scoured from this hole was deposited as a low



mid-channel bar. Flow acceleration over this feature generated a second zone of bed scour at the lower end of the survey reach. This set of bedforms closely resembled a classic pool-riffle sequence (Knighton, 1984), although there was no obvious sediment grain size sorting in the model.

The 0.3 m element created the most extensive and deepest scour hole (12 mm of net scour) because it blocked and subducted the fastest moving body of flow near the free surface. The scoured sediment was then deposited as a large mid-channel bar, which extended across the full width of the channel bed up to a maximum height of 14 mm. Flow acceleration over this bar produced an equally large zone of secondary bed scour towards the downstream end of the survey reach. The channel adjustments caused by the 0.3 m element are shown in Plate 6.



**Plate 6: Channel adjustment caused by the 0.3 m debris element**

The extent and depth of bed scour is therefore seen to be a function of debris element size and also position with respect to the velocity profile (both vertically from the bed and laterally across the channel). Large elements and/or elements near to the center of the



channel and high in the velocity profile cause a greater depth and extent of scour than smaller elements and/or elements near to the channel bed and banks. The size of mid channel, alternate and lateral bars is proportional to the volume of material eroded from the scour holes.

#### **7.10 Geomorphic results: Prototype**

Because the flume is a fully scaled model the geomorphic results can be scaled to prototype dimensions, and compared directly with the field results, rather than having to resort to comparison by ‘similarity of process’ (Cherry and Beschta, 1986; Young, 1991; Peakall et al., 1996; Braudrick et al., 1997). The flume survey data was therefore scaled to prototype dimensions using the X and Y scaling relationships defined by the model ( $X_r = 59.667$ ;  $Y_r = 27.142$ ). The rescaled data were then converted to contour plots. The resulting channel topographies are shown in Figures 18 and 19. Note the difference in scale between Figures 15 and 16 (lengths and depths in cm) and Figures 18 and 19 (lengths and depths in m). The reach length surveyed from the debris element downstream is 60m, and the undisturbed pre-test channel top width is 17.9 m. These surfaces represent the actual scale of features that would be found in the prototype reach of Abiaca Creek caused by each debris element type after 6 hours of immersion in the flow during the 2-year discharge event. However, the key premise behind this experimentation is that the geomorphology associated with LWD jams varies in a predictable manner downstream through the channel network as channel width increases. Channel width increases in a predictable manner (through the use of regime equations) or can be estimated through the knowledge of other important processes (channel evolution models) with distance downstream through the drainage basin.

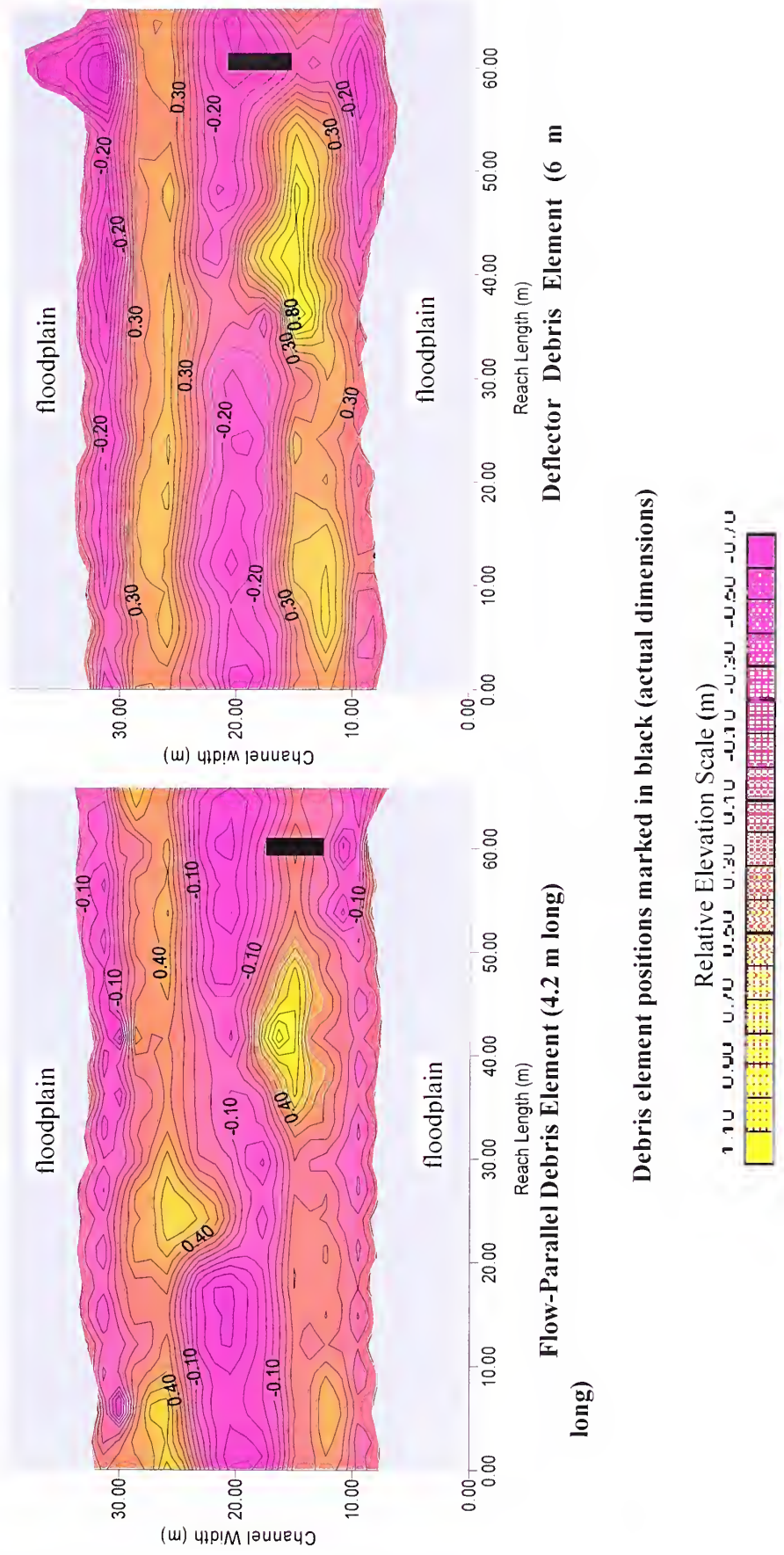
As long as the average ratio between channel width and debris length that characterizes each jam type was reproduced by varying debris length, the suite of geomorphic forms generated should be the same as those found in the field. Although the model had to be scaled from a particular field site, the hydraulic and geomorphic results generated can be regarded to be applicable to any river that has a mobile sand bed and highly erodible banks and similar morphometric and hydraulic characteristics.





The surfaces displayed in Figures 18 and 19 have exactly the same set of features as those in Figures 15 and 16 so it is not necessary to describe their characteristics and mode of formation. The prototype surfaces have, however, been redrawn in a simplified form in Figures 20 and 21, to show the spatial and vertical dimensions of bars and scour holes that can be attributed solely to simple LWD forms in the field.

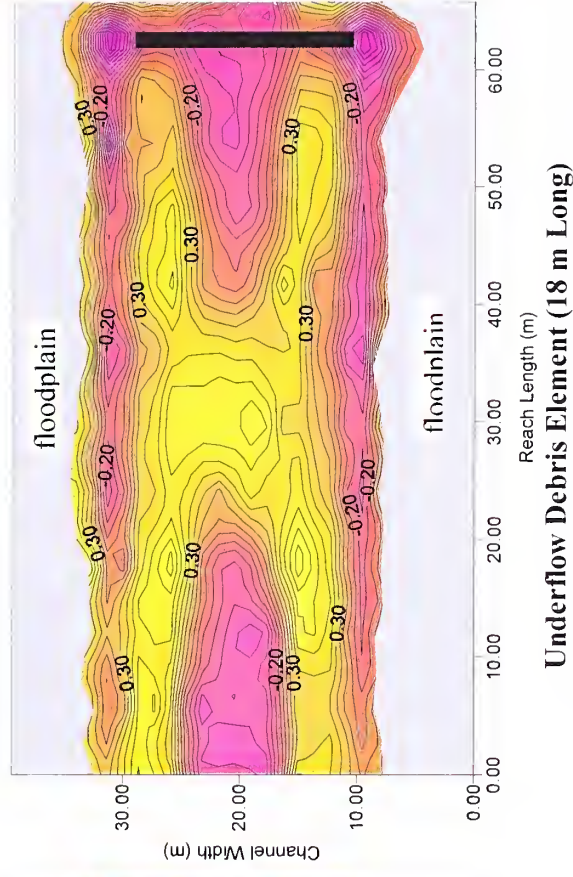
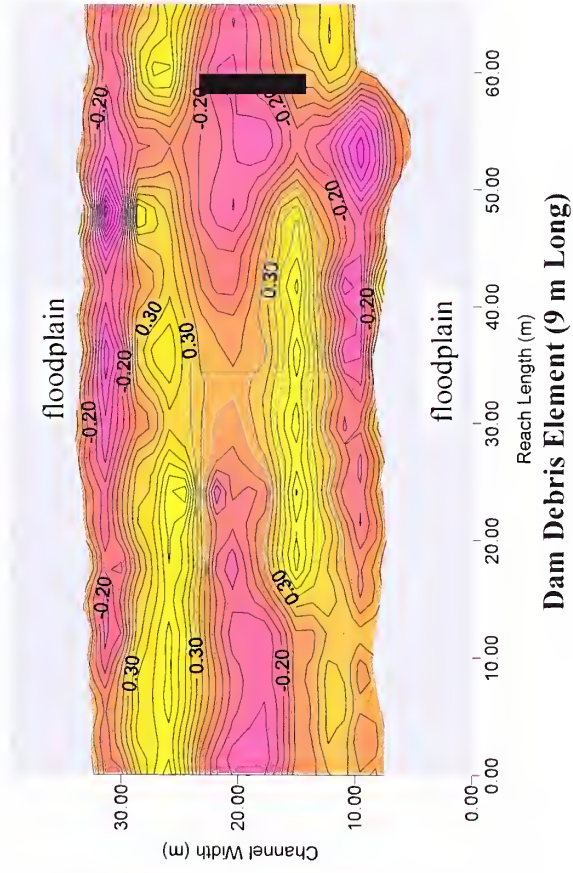




Flow direction is from right to left

**Figure 18: Contour plots of relative depth change calculated for the prototype reach: Flow Parallel and Deflector Debris elements**





Debris element positions marked in black (actual dimensions)

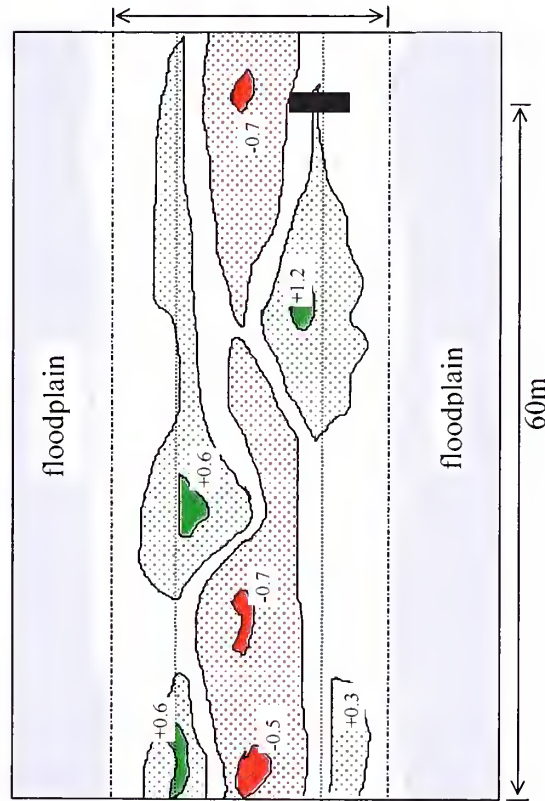


Flow direction is from right to left

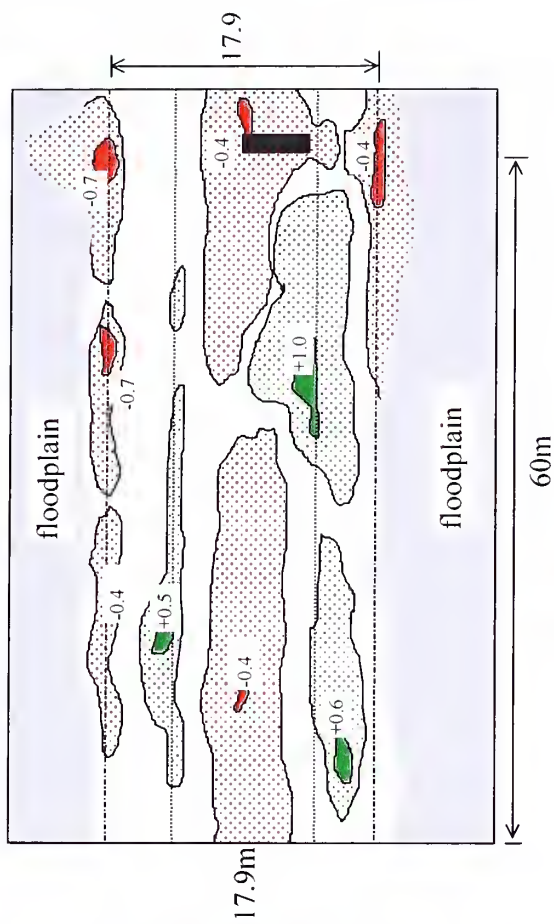
**Figure 19: Contour plots of relative depth change calculated for the prototype reach: Dam and Underflow debris elements**



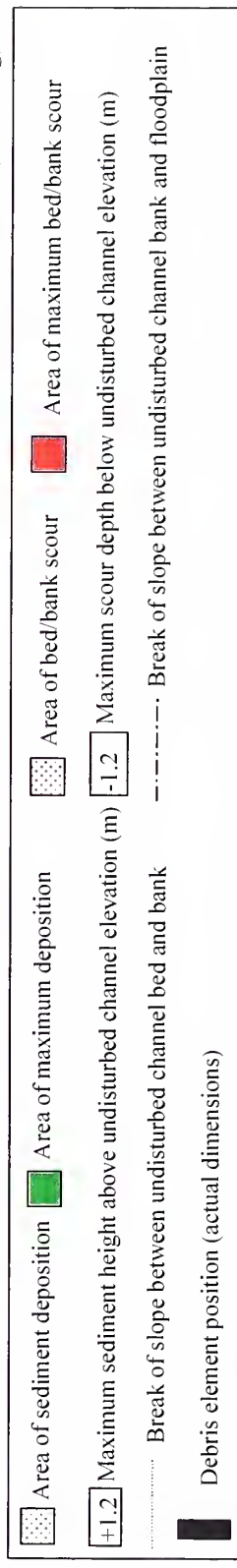




**Flow-Parallel Debris Element (4.2 m long)**



**Deflector Debris Element (6 m long)**



**Figure 20: Geomorphic adjustments to a simple trapezoidal channel caused by 4.2 and 6-m long LWD elements.**





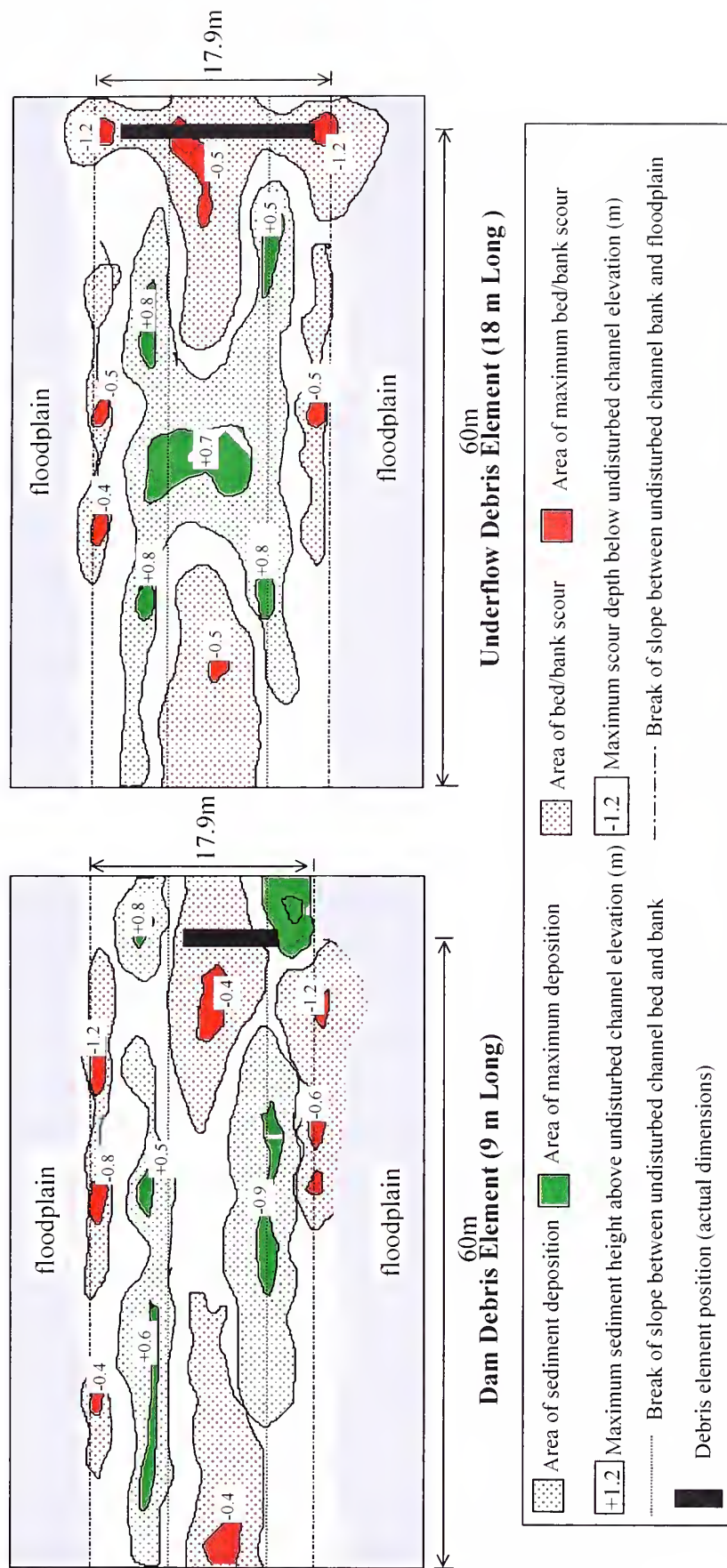


Figure 21: Geomorphic adjustments to a simple trapezoidal channel caused by 9 and 18-m long LWD elements.



## 8 Conclusions

The geomorphic results displayed in Figures 20 and 21 answer a number of questions that have arisen through the course of this research. The results show that LWD has a distinct geomorphic impact upon highly erodible channels, causing both bed scour and bank erosion, and the formation of mid-channel, lateral and alternate bars.

Secondly, the flume results also help to solve the ‘chicken-and-egg’ problem of cause and effect which arises from simple observational geomorphology. In this case, the problem of whether debris jams cause pool-riffle formations or whether debris simply collects where it runs aground against the upstream face of riffles and bars. The geomorphic results clearly demonstrate that, whilst, in some instances debris may be trapped by high points in the channel bed topography, it will also create a distinctive set of geomorphic features regardless of pre-existing channel forms.

Given that the test runs continued until sediment erosion and transport ceased, it is interesting to find that the impact of debris elements is local in nature as the channel becomes progressively less disturbed with distance downstream from each element. Of the three important types of scour (Local, Constriction, and General; see Raudkivi; 1990), only local scour and constriction scour are likely at jams. General scour and degradation were not observed in the flume tests. With regard to the question of channel planform adjustment caused by debris, it is evident from the flume data that even the deflector element did not to cause lateral oscillation of the flow to the extent that meanders developed in the downstream reach.

These conclusions are based solely on the flume results and the limitations of this model must be considered. There was, for example, no sediment transport from upstream, so backwater sediment wedges, which were observed to form upstream of dam type jams in the field, could not form in the model. The model ‘jams’ were composed of single elements whereas ‘real’ jams are usually more complex features so the extent of the geomorphic adjustment in the model may be considerably less than the adjustment that might be caused by large and compact (watertight) jams in the field. Indeed, some authors

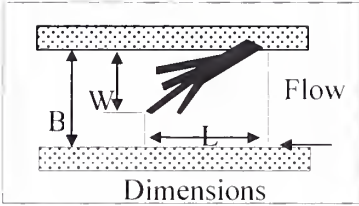

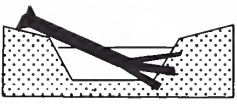

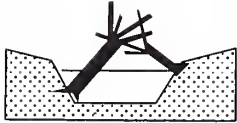


have reported debris jams that have caused channel avulsion (Keller and Swanson, 1979). Because the model bank materials were composed only of sand, it is not known whether the extent of bank erosion would be greater (further into the floodplain) or less had bank failure taken place through both fluvial erosion and by mass failure. However the results presented herein represent the simplest geomorphic forms that the field scientist can expect to see in association with the different jam types encapsulated in the Debris Jam Classification Model.



## APPENDIX

Large Woody Debris Formation Survey used by Smith and Shields (1992)

Stream Name _____ Reach _____ Information _____ _____ Date _____ Time _____		 <p>Dimensions</p>																							
<p style="text-align: center;">Width-Perpendicular to Flow Direction</p> <table border="1" style="width: 100%; border-collapse: collapse;"> <tr> <td style="width: 33%; text-align: center;"><math>W &lt; B/4</math></td> <td style="width: 33%; text-align: center;"><math>B/4 &lt; W &lt; B/2</math></td> <td style="width: 33%; text-align: center;"><math>B/2 &lt; W &lt; B</math></td> </tr> <tr> <td style="text-align: center;"><math>L &lt; B/2</math></td> <td></td> <td></td> </tr> <tr> <td style="text-align: center;"><math>B/2 &lt; L &lt; B</math></td> <td></td> <td></td> </tr> <tr> <td style="text-align: center;"><math>L &gt; B</math></td> <td></td> <td></td> </tr> </table> <p style="text-align: center;">Length-Parallel to Flow Direction</p>  <p style="text-align: center;"><b>TYPE A: COLLAPSED BRIDGE</b></p>	$W < B/4$	$B/4 < W < B/2$	$B/2 < W < B$	$L < B/2$			$B/2 < L < B$			$L > B$			<p style="text-align: center;">Width-Perpendicular to Flow Direction</p> <table border="1" style="width: 100%; border-collapse: collapse;"> <tr> <td style="width: 33%; text-align: center;"><math>W &lt; B/4</math></td> <td style="width: 33%; text-align: center;"><math>B/4 &lt; W &lt; B/2</math></td> <td style="width: 33%; text-align: center;"><math>B/2 &lt; W &lt; B</math></td> </tr> <tr><td></td><td></td><td></td></tr> <tr><td></td><td></td><td></td></tr> <tr><td></td><td></td><td></td></tr> </table>  <p style="text-align: center;"><b>TYPE B: RAMP</b></p>	$W < B/4$	$B/4 < W < B/2$	$B/2 < W < B$									
$W < B/4$	$B/4 < W < B/2$	$B/2 < W < B$																							
$L < B/2$																									
$B/2 < L < B$																									
$L > B$																									
$W < B/4$	$B/4 < W < B/2$	$B/2 < W < B$																							
<table border="1" style="width: 100%; border-collapse: collapse;"> <tr><td></td><td></td><td></td></tr> <tr><td></td><td></td><td></td></tr> <tr><td></td><td></td><td></td></tr> </table> <p style="text-align: center;">Length-Parallel to Flow Direction</p>  <p style="text-align: center;"><b>TYPE C: DRIFT</b></p>										<table border="1" style="width: 100%; border-collapse: collapse;"> <tr><td></td><td></td><td></td></tr> <tr><td></td><td></td><td></td></tr> <tr><td></td><td></td><td></td></tr> </table>  <p style="text-align: center;"><b>TYPE D: STREAMBANK</b></p>															





## REFERENCES

- Alam A.M. and Kennedy J.F. (1969), "Friction factors for flow in sand-bed channels", *J. Hydraul. Div. ASCE*, 95(HY6), 1973-1992.
- Allen J. (1947), *Scale Models in Hydraulic Engineering*, Longmans, Green & Co, New York.
- Barnes H.H. (1967), "Roughness Characteristics of Natural Channels", *U.S. Geol. Surv. Water-Supply Paper no. 184*.
- Bevan K., Gilman K. and Newson M. (1979), "Flow and flow routing in upland channel networks", *Hydrol. Sci. Bull.*, 24, 303-325.
- Blench T. (1955), "Scale relations among sand-bed rivers including models", *Proc. Hydraul. Div. ASCE*, 81(Apr), no. 667.
- Bodron J.A. (1994), "Development of a dynamic routing model to assess the effects of large woody debris removal", M.Sc. Thesis, University of Memphis, Tennessee.
- Braudrick C.A., Grant G.E., Ishikawa Y. and Ikeda H. (1997), "Dynamics of wood transport in streams: A flume experiment", *Earth Surf. Proc. Landf.*, 22, 669-683.
- Chadwick A. and Morfet J. (1991), *Hydraulics in Civil Engineering*, Harper Collins Academic, Boulder.
- Cherry J. and Beschta R.L. (1986), "Coarse woody debris and channel morphology: A flume study", *Water Resour. Bull.*, 25(5), 1031-1037.
- Chow V.T. (1959), *Open Channel Hydraulics*, McGraw-Hill, New York.
- Einstein H.A. and Chien N. (1954), "Similarity of distorted river models with movable bed", *Proc. Hydraul. Div. ASCE*, 80(Dec), no. 566.
- Gippel C.J., O'Neil I.C. and Finlayson B.L. (1992), "The hydraulic basis of snag management", Rep. Ctr. for Environ. Appl. Hydro., Dept. of Civ. and Environ. Eng., University of Melbourne, Australia.
- Gregory K.J., Gurnell, A.M. and Hill C.T. (1985), "The permanence of debris dams related to river channel processes", *Hydrol. Sci. J.*, 30, 3-9.
- Henderson F.M. (1966), *Open Channel Flow*, MacMillan, New York.
- Keller E.A. and Swanson F.J. (1979), "Effects of large organic material on channel form and fluvial processes", *Earth Surf. Proc. Landf.*, 4, 361-381.
- Knighton D. (1984), *Fluvial Forms and Processes*, Chapman and Hall, Inc., London.



- MacDonald A. and Keller E.A. (1987), "Stream channel response to removal of large woody debris, Larry Damm Creek, N. W. California", *Erosion and Sedimentation in the Pacific Rim*, IAHS Publ. no. 165, 405-407.
- Marston R.A. (1982), "The geomorphic significance of log steps in forest streams", *Ann. Assoc. Am. Geog.*, 72, 99-108.
- Novak P. and Cabelka J. (1981), *Models in Hydraulic Engineering: Physical Principles and Design Applications*, Pitman, Boston.
- Peakall J. and Warburton J. (1996), "Surface tension in small hydraulic river models: the significance of the Weber number", *J. Hydrol. (NZ)*, 35, 199-212.
- Peakall, J., Ashworth P.J. and Best J.L. (1996), "Physical modeling in fluvial geomorphology: Principles, applications and unresolved issues", *The Scientific Nature of Geomorphology*, Rhoads, B.L. and Thorn, C.E. (Eds.), John Wiley & Sons Ltd, Chichester, 221-253.
- Petryk S. and Bosmajian G. (1975), "Analysis of flow through vegetation", *J. Hydraul. Div. ASCE*, 101(HY7), 871-884.
- Raudkivi A.J. (1990), *Loose Boundary Hydraulics*, Pergamon Press, Oxford.
- Richards K.R. (1982), *Form and Process in Alluvial Channels*, Methuen & Co., London.
- Roberson J.A. and Crowe C.T. (1993), *Engineering Fluid Mechanics: Fifth edition*, John Wiley & Sons Inc, New York.
- Schumm S.A., Harvey M.D. and Watson C.C. (1984), *Incised Channels: Morphology, Dynamics and Control*, Water Resources Publication, Littleton, Colorado.
- Shields, F.D. and Gippel, C.J. (1995), "Prediction of effects of woody debris removal on flow resistance", *J. Hydraul. Eng.*, 121, 341-354.
- Shields F.D. and Nunnally N.R. (1984), "Environmental aspects of clearing and snagging", *J. Environ. Eng.*, 110(1), 153-165.
- Smith R.H. and Shields F.D. (1992), "Incremental effects of large woody debris removal on physical aquatic habitat", *U.S. Army Corps of Engineers Technical Report EL-92-35*.
- Summerfield M.A. (1991), *Global Geomorphology*, Longman Scientific & Technical, co-published with John Wiley & Sons Ltd, Chichester.



- Swanson F.J. and Leinkaemper G.W. (1978), "Physical Consequence of Large Organic Debris in Pacific Northwest Streams", *U.S.D.A. Forest Service General Technical Report PNW-69*.
- Thorn C.E. (1988), *Introduction to Theoretical Geomorphology*, Unwin Hyman, Boston.
- Vanoni V.A. (1966), "Progress Report Task committee on Preparation of Sedimentation Manual, Committee on Sedimentation Sediment Transportation Mechanics: Initiation of Motion", *J. Hydraul. Div. ASCE*, 92(HY2), 291-314.
- Wallerstein N., Thorne C.R. and Doyle M.W. (1997), "Spatial distribution and impact of large woody debris in northern Mississippi", *Management of Landscapes Disturbed by Channel Incision*, Wang, S.S.Y., Langendoen, E.J. and Shields, F.D. Jr. (Eds.), University of Mississippi Press.
- Watson C.C., Abt S.R., Thorne C.R., Gessler D., Van Zanten B.L. and Hendon S.L. (1993), "Demonstration Erosion Control Project, 1993 Monitoring Sites Evaluation", *Colorado State University*, submitted to U.S. Army Corps of Engineers, Waterways Experiment Station, Vicksburg, Mississippi.
- White F.M. (1979), *Fluid Mechanics*, McGraw-Hill, New York.
- White F.M. (1994), *Fluid Mechanics: Third edition*, McGraw-Hill, New York.
- Wolman M.G. (1955), "The natural channel of Brandywine Creek", *U.S. Geol. Surv. Prof. Paper* 271.
- Yalin M.S. (1971), *Theory of Hydraulic Models*, Macmillan, New York.
- Young W.J. (1991), "Flume study of the hydraulic effects of large woody debris in lowland rivers", *Reg. Rivers*, 6, 203-211.





